

# **Final Report for NASA Grant # US/NASA/NAG-1-020**

## **Part I**

### **Resonant Spectra of Malignant Breast Cancer Tumors Using the Three-Dimensional Electromagnetic Fast Multipole Model**

Magda El-Shenawee

Department of Electrical Engineering  
University of Arkansas  
Fayetteville, AR 72701  
Tel: 501-575-6582, Fax: 501-575-7967  
[magda@uark.edu](mailto:magda@uark.edu)

#### **ABSTRACT**

An intensive numerical study for the resonance scattering of malignant breast cancer tumors is presented. The rigorous three-dimensional electromagnetic model, based on the equivalence theorem, is used to obtain the induced electric and magnetic currents on the breast and tumor surfaces. The results show that a non-spherical malignant tumor can be characterized based on its spectra regardless of its orientation, the incident polarization, or the incident or scattered directions. The tumor's spectra depend solely on its physical characteristics (i.e., the shape and the electrical properties), however, their locations are not functions of its burial depth. This work provides a useful guidance to select the appropriate frequency range for the tumor's size.

#### **I. INTRODUCTION**

Extensive scientific research has been conducted in recent years to defeat the breast cancer, however, this disease remains a potential life threatening for many women. Several imaging modalities were developed and used to detect the breast cancer, e.g., the X-ray mammography, which currently is considered the most reliable method, the ultrasound, the magnetic resonance imaging, and others as reviewed in [1]-[2]. Recently, microwave tomography has been shown a

promise for early detection of breast cancer [3]-[8], in addition, the microwave imaging has been used in several medical applications [9]. The electrical properties of the normal breast tissues, the benign and/or the malignant tumors and the breast skin layer represent key issues for this technique. Measurements of the electric dielectric constants of these tissues over a range of frequencies are reported in the literature [10]-[17]. The microwave radar technology has been investigated in detecting and imaging the malignant breast tumors [18]-[24]. In these papers, the computational electromagnetic method, the finite difference time domain (FDTD), along with signal processing techniques were used to simulate and analyze several microwave systems leading to interesting and promising results.

In our previous research on the humanitarian anti-personnel mine detection application using the ground penetrating radar (GPR), it was very difficult to distinguish between the scattered signal from the rough ground where a small plastic mine was buried and the scattered signal from the ground without buried mines [25]-[28]. This difficulty was due to the small size of the mine relative to the wavelength, the soil medium was very lossy in some cases, and the mine's electrical properties were very similar to those of the surrounding ground when the soil was dry. In addition, the considerable clutters due to the presence of the random rough ground, the soil inhomogeneities and the presence of benign objects nearby the target, greatly obscured the detection process.

Similarly, in the breast cancer application, several difficulties can be encountered such as; the normal breast tissues are very lossy at the microwave frequencies, compared with the soil in GPR applications [25]-[28]; the small size of the tumor for the early detection purpose; and the heterogeneities of the breast tissues. These factors make detecting the tumor in the breast as difficult as sensing the plastic target in the minefield.

Several researchers had reported that the dielectric and conducting objects could resonate at certain frequencies in the electromagnetic spectrum [29]-[40]. When these frequencies are independent of the excitation, they are located in the complex plane and called the natural frequencies. Their locations depend only on the object's size, shape, and material. On the other hand, these objects can also resonate upon excitation by a continuous wave at real frequencies as reported in [29], where Mie solution was used. The resonating objects were located in the free space in [29]-[37], while they were buried beneath an interface in [18], [38]-[40]. In [29], the immersed object in free space was excited by plane waves, and the scattered radiation was monitored as function of the frequency in order to obtain their resonance spectrum. This approach is adopted here to obtain the resonance spectra of the malignant tumors buried in the lossy normal breast tissues, as initiated in [18]. In this situation, the malignant tumors act as low Q-resonators since their dielectric constants are lossy as well. Moreover, the magnitude of the scattered waves at the resonant frequencies is considerably reduced due to the large absorption of the transmitted waves in breast tissues. However, these scattered fields exhibit an obvious resonant radiation when a tumor is present in the breast. It is important to emphasize that the current work is focused on objects buried under an interface, i.e. inhomogeneous lossy medium, while the work presented in [29] was focused on lossless dielectric objects immersed in the free space. While, the Mie solution was used in [29], a frequency-domain fast computational electromagnetic technique is used in this work. This technique is based on the fast multipole method hybridized with the steepest descent integration rule (SDFMM) [41]-[44], [25]-[28]. In particular, the multiple interaction method (MIM) combined with the SDFMM (MIM-SDFMM [45]) is employed in this work, with using the method of moments (MoM) only for validation.

The formulations of the electromagnetic model are discussed in Section II, the numerical results are presented in Section III and the concluding remarks are summarized in Section IV.

## II. METHODS

The rigorous 3-D electromagnetic model, based on the classical equivalence theorem, is used to simulate scattering from malignant tumors buried in normal breast tissues. This model was successfully implemented in the humanitarian anti-personnel plastic mine detection applications [25]-[28]. Basically, the surfaces of the breast and the tumor are discretized using the RWG (Rao, Wilton, Glisson) triangular patches [46]. Upon approximating the induced equivalent surface currents using the vector basis functions and testing the integral equations with the same basis functions; a set of linear system of equations was obtained as [25],[47]:

$$\begin{pmatrix} \bar{Z}_{S,S} & \bar{Z}_{S,T} \\ \bar{Z}_{T,S} & \bar{Z}_{T,T} \end{pmatrix} \begin{pmatrix} \bar{I}_S \\ \bar{I}_T \end{pmatrix} = \begin{pmatrix} \bar{V}_S \\ 0 \end{pmatrix} \quad (1)$$

This system of equations incorporates all the interactions between self-elements on the breast surface ( $\bar{Z}_{S,S}$ ), elements on the breast and the tumor surfaces ( $\bar{Z}_{S,T}$  and  $\bar{Z}_{T,S}$ ), and self-elements on the tumor surface  $\bar{Z}_{T,T}$ . The vector  $\bar{V}_S$  represents the incident tangential electric and magnetic fields on the breast surface. This system of equations needs to be solved for the unknown current coefficients  $\bar{I}_S$  and  $\bar{I}_T$ , excited on the breast and tumor surfaces, respectively.

Solving (1) using the MoM would be computationally very expensive, however, the MoM will be used for validation. The first method to solve (1) is to implement the complete SDFMM, which could be inefficient computationally for large burial depths of the tumor. The second method to solve (1) is to implement the MIM-DFMM as discussed in [45]. Basically, the later method solves two separate linear systems of equations for the unknown coefficients while exploiting an iterative procedure to update the incident fields on both the breast surface ( $S$ ) and the tumor surface ( $T$ ). These two systems of equations are given by [45]:

$$\bar{Z}_{S,S} \bar{I}_S^{(n)} = \bar{V}_S^{(n)} \quad (2a)$$



$$\bar{Z}_{T,T} \bar{I}_T^{(n)} = \bar{V}_T^{(n)} \quad (2b)$$

in which  $n$  represents the number of multiple interactions between the tumor and the breast surface,  $n = 0, 1, \dots$ , where  $n = 0$  implies that the induced currents on the breast surface are due only to the illuminating source and no interaction took place with the tumor. The algorithm starts by assuming no buried tumors are present in the breast and solving (2a) for the unknown coefficients on the breast surface, i.e.  $\bar{I}_S^{(0)}$ . These coefficients are induced due to the tangential incident fields  $\bar{V}_S^{(0)}$ . Consequently, the induced electric and magnetic currents on the breast surface, i.e.  $\bar{J}_S^{(0)}$  and  $\bar{M}_S^{(0)}$ , excite the buried tumor with the fields  $\bar{V}_T^{(1)}$  in (2b). These fields are calculated using the near-field surface integrations given by [48]:

$$\bar{H}_T^A(x, y, z) = -\frac{1}{4\pi} \iint_{S'} (\hat{R} \times \bar{J}_s(x', y', z')) \frac{1+ikR}{R^2} \exp(-ikR) dS', \quad \bar{E}_T^A(x, y, z) = \frac{1}{i\omega\epsilon} \nabla \times \bar{H}_T^A \quad (3a)$$

$$\bar{E}_T^F(x, y, z) = -\frac{1}{4\pi} \nabla \times \iint_{S'} \bar{M}_s(x', y', z') \frac{\exp(-ikR)}{R} dS', \quad \bar{H}_T^F(x, y, z) = -\frac{1}{i\omega\mu} \nabla \times \bar{E}_T^F \quad (3b)$$

where the total electric and magnetic fields are  $(\bar{E}^A + \bar{E}^F)$  and  $(\bar{H}^A + \bar{H}^F)$ , respectively, the fields associated with the vector potentials  $\bar{A}$  and  $\bar{F}$  are represented by the superscripts  $A$  and  $F$ ,  $\hat{R}$  is a unit vector between the source and observation points with length  $R$ , and  $k$  is the wave number of the surrounding medium with permittivity and permeability  $\epsilon$  and  $\mu$ , respectively, and  $dS'$  is the differential surface element on the breast. The next step is to solve (2b) for the unknown coefficients, i.e.  $\bar{I}_T^{(1)}$ , in order to obtain the electric and magnetic currents on the tumor surface,  $\bar{J}_T^{(1)}$  and  $\bar{M}_T^{(1)}$ , respectively. This process is to be repeated till the surface current solutions converge.

The other advantages of using the MIM-SDFMM is its capability to calculate the contribution of each wave interaction between the tumor and the breast interface, which provides

a good insight to the scattering mechanism involved. Moreover, it enables calculating the induced surface currents on the breast due to only the presence of the tumor [45]. This implies that no subtraction process is used in this work to obtain the tumor's signature, which leads to faster and more efficient results. The SDFMM is used to solve (2a) which is associated with the breast surface, where the impedance matrix  $\bar{Z}_{s,s}$  is converted to a sparse one. It is important to mention that the order of matrix  $\bar{Z}_{s,s}$  is much large than the order of the impedance matrix  $\bar{Z}_{t,t}$ , which is associated with the tumor's surface. This is due to the small size of the tumor compared with the breast surface. Therefore, it is more efficient to use the MoM to solve (2b). The computational complexity of the MIM-SDFMM is discussed in detail in [45].

The electric and magnetic currents induced on the breast surface due to just the tumor are  $\bar{J}_s = \bar{J}_s^{(1)} + \bar{J}_s^{(2)} + \dots + \bar{J}_s^{(n)}$ , and  $\bar{M}_s = \bar{M}_s^{(1)} + \bar{M}_s^{(2)} + \dots + \bar{M}_s^{(n)}$ , respectively. Notice, that the driving surface currents  $\bar{J}_s^{(0)}$  and  $\bar{M}_s^{(0)}$ , are induced on the breast due to only the illuminating source (i.e. transmitting antenna), assuming that no tumors are buried in the breast.

In this work, the thickness of the breast skin (i.e., the skin layer) and inhomogeneities are not incorporated in the electromagnetic model discussed above. However, the model includes an interface between the air and breast tissues where the tumor is buried (i.e., accounts for three different homogeneous regions). The numerical results in Section III are based on computing the scattered intensity represented by the radar cross section (RCS) defined as  $(4\pi r^2 |\bar{E}^s|^2 / 2\eta_0 P^i)$  [48], where  $\bar{E}^s$  is the scattered electric field,  $P^i$  is the incident power [49], and  $r$  is the distance from the scatterer to the observation point.

It is important to emphasize that the SDFMM is a surface integral equation based algorithm as derived and discussed in [25]-[28], [43]-[45]. There is no restriction on the object's shape as

long as its surface can be discretized into triangular patches, which needs special software for this discretization. Moreover, the SDFMM does not rely on the object's symmetry similar to other MoM based models, e.g. [39], however, the SDFMM cannot be used to simulate a region if the dielectric constant is varying gradually from one point to another. In this case, the volume integral equations should be used instead, where the scatterer's volume is discretized into volumetric elements. The main advantage of the SDFMM is its  $O(N)$  computational complexity for both the CPU time and computer memory, where  $N$  is the total number of surface current unknowns, compared with the MoM that requires  $O(N^2)$  to solve the same problem.

Several key issues will be discussed in detail such as the electrical properties of breast tissues, the geometry of the breast and the spectrum of spheres immersed in air or buried beneath an interface. These issues are discussed in depth as follows:

**i. Electrical properties of breast tissues:**

The relative dielectric constants of the malignant tumor and normal breast tissues are obtained from the reported measurements in the literature [10]-[17]. The frequency dependence of the dielectric constants ( $\epsilon_r = \epsilon' - j\epsilon''$ ) for the normal breast tissues and malignant tumor are plotted in Fig. 1 versus the frequency from 1 to 10 GHz. These results are calculated using equation (1) in Ref. [20], which was obtained by curve fitting the published measured data up to 3GHz. A variety of dielectric constants either obtained from the actual measurements data [10]-[17] or from the curve fitted data of Fig. 1, will be used in Section III.

**ii. Breast geometry:**

Two different geometries for the breast are simulated in this work as shown in Figs. 2a-b. In Fig. 2a, the breast surface is assumed flat which represents an ideal situation [18]. However, in Fig. 2b, the breast surface is simulated as a 3-D curved geometry which can represent a patient

lying on her back [20]-[21]. If the patient is lying on her stomach, the breast will have more curved geometry (more cylindrical shape) [22]-[23], which will not be considered in this work.

### iii. Validation with Mie's solution in [29]:

It is important to examine the resonant radiation of just a dielectric sphere immersed in air, before investigating the more complicated scatterer that contains a sphere buried in a different medium as shown in Figs. 2a-b.

In Example 1, three dielectric constants of the sphere are assumed as  $\epsilon_r = 50$  (lossless),  $\epsilon_r = 36$  (lossless [29]) and  $\epsilon_r = 50 - j12$  (lossy) as shown in Fig. 3. The RCS is plotted versus the parameter  $ka$ , where  $a$  is the radius of the sphere,  $k = 2\pi/\lambda_0$ ,  $\lambda_0 = 3 \times 10^8 / f$  (m) is the free space wavelength, and  $f$  is the frequency of the incident waves. These results are obtained using the MoM where the sphere is discretized into 764 triangular patches leading to 2292 electric and magnetic unknown coefficients. The plane wave is used for excitation at normal incidence ( $\theta' = 0^\circ$ ) with the electric field is in the  $x$ -direction as shown in Fig. 3. The electric field in this case is parallel to the plane of incidence ( $z$ - $x$  plane), which represents the vertical polarization (V-pol.). All results of Fig. 3 are for the co-polarized scattered waves in the backscatter direction. The results show that the RCS of the lossless spheres exhibits a sharp resonant scattering upon varying the parameter  $ka$ . The results of the lossless sphere with  $\epsilon_r = 36$ , show full agreement with those obtained using the Mie solution and reported in [29]. Notice that the magnitude of the RCS is tremendously reduced when the sphere becomes lossy ( $\epsilon_r = 50 - j12$ ). Moreover, the very sharp peaks obtained for the lossless sphere at the resonant frequencies are not shown in lossy case. The relative dielectric constant of  $\epsilon_r = 50 - j12$  simulates the electrical property of a malignant tumor which implies that  $\epsilon'_r = 50$  and the

conductivity  $\sigma = \omega\epsilon''/\epsilon_0 = 4.0 S/m$  at  $f = 6$  GHz [18], [19], [22]. The results show that the magnitude of resonance spectra of the lossy sphere is much smaller than those of the lossless one.

**iv. Effect of the presence of an interface:**

In Example 2, the effect of the presence of an interface on the observed resonant scattering is investigated. A lossless sphere with  $\epsilon_{r,3} = 50$  is buried at depth  $d$  measured from its center beneath the flat interface of Fig. 2a. The surrounding medium is slightly lossy with  $\epsilon_{r,2} = 2 - j0.1$ . To eliminate edge excitations, the interface is excited using plane waves tapered towards the edges of the flat surface, i.e. using a Gaussian beam as discussed in [25], [50]. The incident waves are in the normal direction with the electric field in the  $y$ -direction, i.e. perpendicular to the plane of incidence ( $z$ - $x$  plane), which represents the horizontal polarization (H-pol.). The RCS for just the buried sphere is plotted vs  $ka$  in the backscatter direction as shown in Fig. 4.

The dimensions of the modeled flat surface (i.e.  $L_x \times L_y$ ) are  $2.94\lambda_0 \times 2.94\lambda_0$  and the sphere's location is centered with burial depths  $d = -0.3\lambda_0$  and  $d = -0.6\lambda_0$  as shown in Fig. 4. The incident Gaussian beam used in this work has width equal to  $1.2\lambda_0$ . The flat interface is discretized into 4,802 triangular patches (i.e., discretization rate is  $0.06\lambda_0$ ) leading to 14,210 electric and magnetic unknown coefficients. For each value of the depth  $d$ , the MIM-SDFMM computer code was executed 81 times for the values of  $ka$  from 0.2 to 1 in steps of 0.01.

In Fig. 4, the RCS results clearly exhibit sharp peaks at certain values of the parameter  $ka$  despite of the presence of the interface. It is important to mention that finer resolution for  $ka$  could lead to increasing the magnitude of some of these sharp peaks. As the burial depth

increases to  $d = -0.6\lambda_0$ , the magnitude of the sharp peaks is accordingly reduced as shown in the figure.

**v. Computational issues:**

It is important to emphasize that varying the parameter  $ka$  in each run requires solving both (2a) and (2b) only once except when the computer code starts, then it requires solving (2a) twice. This leads to saving more than 30% of the computation time. The total CPU required to obtain the solutions using the Compaq Alpha Server (GS140 EV6) with 667 MHz clock speed is approximately 22 hrs for each full plot in Fig. 4 (i.e., for each 81 runs). Moreover, to speed up the computations, only a single interaction between the sphere and the interface is considered (i.e.,  $n = 1$ ) as discussed earlier. The MIM-SDFMM is tested when more interactions are considered (i.e. for  $n = 2, 3, \dots$ , not presented here), leading to insignificant differences due to the higher order interactions. This observation was proved in [45], particularly, when the surrounding medium was lossy. This justifies accounting for only the first interaction, i.e.  $n=1$ , in all numerical results presented in Section III.

### **III. NUMERICAL RESULTS**

Several examples for the resonance spectra of malignant tumors buried in normal breast tissues are presented in this section through out Examples 3-9. In these examples, the effect of tumor's shape, burial depth, electrical properties and orientation on the resonance spectra are investigated. Moreover, the output of changing the electrical properties of normal breast tissues and breast geometry, the polarization, the direction and the frequency of the incident electromagnetic wave is presented as well. The investigations are discussed as follows:

**i. Tumor's burial depth:**

In Example 3, a lossy medium is assumed in order to simulate the normal breast tissues properties at the microwave frequencies. The dielectric constant is  $\epsilon_{r_2} = 9.0 - j1.2$  which implies that  $\epsilon'_r = 9.0$  and  $\sigma = 0.4 \text{ S/m}$  at  $f = 6 \text{ GHz}$  [18], [19], [22]. The lossy sphere of dielectric constant  $\epsilon_{r_3} = 50 - j12$  to simulate the malignant tumor is buried under the flat interface of Fig. 2a, at a variety of depths from  $d = -0.3\lambda_0$  to  $d = -0.7\lambda_0$ , the results are shown in Fig. 5a. The co-polarized backscattered RCS for just the tumor clearly exhibits a resonance scattering even when it is buried in such a lossy medium. These results show that the buried tumor's resonance phenomenon survived the interface and the lossy surrounding environment for both burial depths. However, the tumor's burial depth mostly affects the magnitude of the spectra and not the resonance locations.

**ii. Variety of electrical properties:**

It is also important to investigate a variety of the breast and tumor electrical properties on the resonant scattering as shown in Fig. 5b. The dielectric values are obtained from the measurements reported in the literature as (i)  $\epsilon_{r_2} = 9.0 - j1.2$ ,  $\epsilon_{r_3} = 50.0 - j12$  at  $f = 6 \text{ GHz}$  [18], [19], [22], (ii)  $\epsilon_{r_2} = 10 - j1.97$ ,  $\epsilon_{r_3} = 45 - j16.87$  at  $f = 3.2 \text{ GHz}$  (the lower limit values reported in table 5 in [14]), (iii)  $\epsilon_{r_2} = 9.8 - j2.08$ ,  $\epsilon_{r_3} = 46 - j25.87$  at  $f = 3.2 \text{ GHz}$  (for patient no. 37 reported in Table 2 in [14]), (iv)  $\epsilon_{r_2} = 15 - j3.6$ ,  $\epsilon_{r_3} = 52 - j18.4$  at  $f = 1 \text{ GHz}$  reported in [16], and (v)  $\epsilon_{r_2} = 25 - j5.9$ ,  $\epsilon_{r_3} = 60 - j22.49$  at  $f = 3.2 \text{ GHz}$  (the upper limit values reported in Table 5 in [14]). As expected, when the normal breast tissues become more lossy, the scattering magnitude at the resonant frequencies (i.e., the maximum points) decreases accordingly as shown in Fig. 5b.

### iii. Multiple frequency:

In Example 4, the resonant scattering is investigated vs the frequency from 1 to 10 GHz. The dielectric constants presented in Fig. 1 are used in this example [20]. Notice that the real and imaginary parts of the dielectric constants of normal breast tissues are almost constant in this range of frequency, which is not the case for the malignant tumor. To speed-up the calculations, only the change in the malignant tumor's dielectric constant with frequency is incorporated in the computer code, keeping the dielectric constant of the normal tissues constant at  $\epsilon_r = 10 - j1.2$  (see Fig. 1). This assumption justifies computing and storing the elements of the breast impedance matrix,  $\bar{Z}_{s,s}$  only once, when the computer code starts, leading to considerable saving of the computation time. In Figs. 6a-b, the backscatter RCS at normal incidence is plotted versus the frequency from 1 to 10 GHz in steps of 100 MHz. The tumor is modeled as a sphere of radius  $a$  ranges from 1 mm to 6 mm, and is buried beneath the flat surface of Fig. 2a at  $d = -1$  cm and  $d = -5$  cm as shown in Figs 6a and 6b, respectively. As expected, the results show that the tumor spectrum varies with the radius  $a$ , however, when the radius becomes 2 mm or less, larger frequency range is required. This indicates the difficulty of detecting small tumors (less than 2 mm) since the surrounding medium becomes more lossy at these high frequencies. Moreover, upon comparing the results of Fig. 6a with those of 6b, it is clear that the tumor's burial depth affects the magnitude of the spectra rather than their locations.

### iv. Incident and scatter directions and polarization:

In Example 5, a variety of incident directions are investigated. The 3-D curved geometry depicted in Fig. 2b is used to simulate the breast in this case. This geometry is assumed to have a sinusoidal shape given by  $H(x, y) = (h_0/2)(\cos(2\pi\rho/\Lambda) + 1)$ ;  $h_0$  is the breast height,  $\rho = \sqrt{(x - \Lambda/2)^2 + (y - \Lambda/2)^2}$  and  $\Lambda = L_x = L_y$  where  $L_x$  and  $L_y$  are the  $x$ - and  $y$ -dimensions,

respectively. In Figs. 7a-c, the RCS for just the spherical tumor is plotted as function of the parameter  $ka$ . The tumor burial depth is  $d = +0.3\lambda_0$  and the breast height is  $h_0 = 0.5\lambda_0$  (see Fig. 2b). In Fig. 7a, the results show the co-polarized RCS for the H-polarization waves with normal incident angle ( $\vartheta^i = 0^\circ$ ). The scattered waves are received at three directions: (i)  $\vartheta^s = 0^\circ$  (backscatter direction), (ii)  $\vartheta^s = 45^\circ, \phi^s = 0^\circ$  (forward direction) and (iii)  $\vartheta^s = 45^\circ, \phi^s = \pi^\circ$  (backward direction). The dielectric constants are assumed to be  $\epsilon_{r2} = 9.0 - j1.2$  for the normal breast tissues and  $\epsilon_{r3} = 50.0 - j12$  for the malignant tumor. As expected, the scattered intensity in the backscatter direction at normal incidence is larger than those in the forward or in the backward directions.

In Figs. 7b and 7c, the co-polarized scattered RCS at the oblique incident direction  $\vartheta^i = 45^\circ, \phi^i = 0^\circ$ , are shown for the H- and V-polarizations, respectively. The results clearly show the resonant scattering for both polarizations and for all three scattering directions ( $\vartheta^s = 0^\circ$ ,  $\vartheta^s = 45^\circ, \phi^s = 0^\circ$ , and  $\vartheta^s = 45^\circ, \phi^s = \pi^\circ$ ). Larger magnitudes were observed in the V-polarization case. For the H-polarization, the magnitude at the resonant frequencies (i.e. the maximum points) occurs almost at the same locations for all three scattering directions as shown in Fig. 7b. However, for the V-polarization case, some of these locations are shifted with changing the scattering direction as shown in Fig. 7c. Interestingly, only in the backscatter direction (i.e.,  $\vartheta^s = 45^\circ, \phi^s = \pi^\circ$ ), the maximum points occur at the same locations for both the H- and V-polarizations.

It is important to mention that the forward direction defined in this work indicates scattering in all directions above the interface, where the receiving antenna should be located (i.e. above the breast surface). This definition is completely different from the forward direction for scattering

from a sphere immersed in free space, which is exactly a  $180^\circ$  from the incident direction as described by Larsen et al in [9]. No resonance was observed in the forward direction in Larsen et al results [9], which is not the case in this work as demonstrated in Figs. 7a-c.

**v. Total scattered intensity and validation with the MoM:**

As discussed in Section II, the above resonant scattering are obtained by calculating the electric and magnetic surface currents induced on the breast surface due to the presence of the malignant tumor. However, the currents induced on the breast surface due to the incident waves (i.e., the transmitting antenna) cannot be differentiated from those induced due to the presence of a tumor. In other words, the surface current induced on the breast is the summation in complex vectors of both currents as discussed in Section II.

Therefore, in Example 6, the total currents induced on the breast surface are used to obtain the total scattering intensity. These results are for the H-polarization at normal incidence with the same dielectric constants and burial depth of Fig. 7. The results clearly exhibit the resonance phenomenon compared with the case where no tumor was present. In order to validate these interesting results, a second multiple interactions between the tumor and the interface (i.e.  $n = 2$ ) is taken into account showing the full agreement with those produced using  $n = 1$ . In addition, the MoM is used to validate both cases demonstrating good agreement with acceptable errors for larger  $ka$ . It is observed in Fig. 8 that the maximum magnitude of the resonance located between  $ka = 0.7$  and  $ka = 0.8$ , is 0.35 compared with 0.015 in Fig. 7a. This is because the same incident power ( $P'$ ) is used to normalize the RCS results in both cases.

**vi. Non-spherical tumor:**

In Example 7, a non-spherical malignant tumor is investigated. In this work, the tumor is assumed to have a prolate spheroid shape. The curved breast geometry depicted in Fig. 2b is

used here, with the dimensions of the prolate spheroid given by  $a$  and  $b$ , where  $a = 2b$ . Three incident directions are used here as; (i)  $\theta^i = 0^\circ$ ; (ii)  $\theta^i = 45^\circ, \phi^i = 0$  and (iii)  $\theta^i = 25^\circ, \phi^i = 130^\circ$ , for both the H- and V-polarizations. The dielectric constants are assumed to be  $\epsilon_{r,2} = 9.0 - j1.2$  for the normal breast tissues and  $\epsilon_{r,3} = 50.0 - j12$  for the malignant tumor. In this example, the original definition of the RCS (i.e.,  $4\pi r^2 |\bar{E}^s|^2 / 2\eta_0 P^i$ ) is used but upon integrating the scattered intensity over the scattering directions in the plane of incidence, i.e.,  $\theta^s = 0^\circ, 1^\circ, 2^\circ \dots, 89^\circ$  at both  $\phi^s - \phi^i = 0^\circ$  (forward direction) and  $\phi^s - \phi^i = 180^\circ$  (backward direction). Then it is normalized with the cross section area  $\pi a^2$ .

In this example, the average of the RCS with respect to the polarization (i.e., the H- and V-polarizations) is processed and plotted versus  $ka$  as shown in Figs. 9a-c. In Fig. 9a, the results are shown for just a malignant tumor horizontally oriented and buried at depth  $d = +0.3\lambda_0$  measured from its center. In this case, the Euler's angles are  $\alpha_x = \beta_y = \gamma_z = 0^\circ$ . On the other hand, in Fig. 9b, the results are shown for the same tumor but randomly oriented and buried at  $d = +0.25\lambda_0$ , with the Euler's angles  $\alpha_x = 10^\circ, \beta_y = 15^\circ, \gamma_z = 5^\circ$ . Interestingly, the results in Figs 9a and 9b show that the resonance occurs approximately at the same values of  $ka$  regardless of the incident angles. However, the results show that the magnitude of these spectra depends on both the incident angle and the object orientation upon comparing Fig. 9a with Fig. 9b.

#### vii. Averaging over incident directions:

The interesting results in Figs. 9a-b suggest that taking the average over the incident direction can produce invariant spectra for the malignant tumor regardless of its orientation as clearly shown in Fig. 9c. Notice that the two spectra shown in Fig. 9c look very similar, except for the magnitude, which is due to the difference in the burial depth ( $0.3\lambda_0$  in Fig. 9a vs  $0.25\lambda_0$  in

Fig. 9b). These results indicate that the spectra of the malignant tumor are invariant with the incident polarization, the incident and scattered directions. However, these spectra depend on the physical characteristics of the tumor, i.e., the shape and the electrical properties of its tissues. These conclusions agree with the results reported in [29] in which lossless objects were immersed in free space. Moreover, the results show that the burial depth mostly affects the magnitude rather than the resonance locations as shown in Fig. 9c. This observation also agrees with the results reported in [39] where the natural resonant frequencies of a mine buried in dispersive layered half space were investigated versus its burial depth. Interestingly, the spherical tumor's spectra shown in Fig. 7 are different from those of the spheroid tumors shown in Fig. 9, which also agrees with the conclusions reported in [29]. This observation can be used to classify the malignant from benign tumors as discussed in [18].

The approach presented in this work can be used to detect and/or discriminate between malignant and benign breast tumors by establishing a library for the spectra of all possible tumor's shapes and tissues. This is feasible using the SDFMM fast model. However, it is essential to investigate the effect of the skin thickness and any breast inhomogeneities on the resonance phenomena. The skin layer is very strong scatterer at the frequency range 1-10 GHz, therefore, including it in the model may change the resonance spectra of the tumor. This issue will be investigated as a future work.

#### IV. CONCLUSIONS

The fast algorithm, MIM-SDFMM, is used in this work to investigate the resonance scattering of the malignant breast cancer tumors. The results show that the resonance scattering phenomenon is invariant with the incident polarization, the incident or scattered directions and the burial depth (except for the magnitude). The spectra vary only with the tumor's shape and

material. This makes the resonance spectrum a unique characteristic for the tumor that can be utilized to detect and/or discriminate between malignant and benign breast tumors, since they differ considerably in shape and material. The results of this work can provide a useful guidance for selecting the frequency range suitable to tumor's characteristics.

### ACKNOWLEDGMENTS

This research was sponsored by the NASA Langley Research Center grant No. US/NASA/NAG-1-020. The author would like to thank W. Lawrence, J. Johnson, M. Deshpande and W. Munden at NASA for their valuable comments and discussions. This work is supported in part by the Northeastern University NSF-ERC award number EEC-9986821.

### REFERENCES

- [1] Manfred Säbel and Horst Aichinger, "Recent developments in breast imaging," *Phys. Med. Bio.* 41, pp. 315-368, 1996.
- [2] K. Großhadern, "Nonmammographic breast imaging techniques," *Current Opinion in Radiology*, no. 4, pp. 146-154, 1992.
- [3] P. M. Meaney, M. W. Fanning, D. Li, S. P. Poplack and K. D. Paulsen, "A clinical prototype for active microwave imaging of the breast," *IEEE Trans. Microwave Theory Tech.*, vol. 11, pp. 1841-1853, 2000.
- [4] P. M. Meaney, K. D. Paulsen, J. T. Chang, M. W. Fanning and A. Hartov, "Nonactive antenna compensation for fixed-array microwave imaging: Part I. Model development," *IEEE Trans. Med. Imag.*, vol. 18, pp. 508-518, June 1999.
- [5] P. M. Meaney, K. D. Paulsen, J. T. Chang, M. W. Fanning and A. Hartov, "Nonactive antenna compensation for fixed-array microwave imaging: Part II. Imaging results," *IEEE Trans. Med. Imag.*, vol. 18, pp. 508-518, June 1999.
- [6] P. M. Meaney, K.D. Paulsen and J. T. Chang, "Near-field microwave imaging of biologically-based materials using a monopole transceiver system," *IEEE Trans. Microwave Theory Tech.*, vol. 46, pp. 31-45, 1998.
- [7] A. E. Souvorov, A. E. Bulyshev, S. Y. Semenov, R. H. Svenson and G. P. Tatsis, "Two-dimensional computer analysis of a microwave flat antenna array for breast cancer tomography," *IEEE Trans. Microwave Theory Tech.*, vol. 48, pp. 1413-1415, August 2000.
- [8] A. E. Bulyshev, A. E. Souvorov, S. Y. Semenov, R. H. Svenson, A. G. Nazarov, Y. E. Sizov and G. P. Tatsis, "Three-dimensional microwave tomography: Theory and computer experiments in scalar approximation," *Inverse Problems*, vol. 16, pp. 863-875, 2000.
- [9] L. E. Larsen and J. H. Jacobi, "Methods of microwave imagery," *Medical Applications of Microwave Imaging*, *IEEE Press*, pp. 118-137, 1986.
- [10] C. Gabriel, S. Gabriel and E. Corthout, "The dielectric properties of biological tissues: I. Literature survey," *Phys. Med. Biol.*, vol. 41, pp. 2231-2249, 1996.

- [11] S. Gabriel, R. W. Lau and C. Gabriel, "The dielectric properties of biological tissues: II. Measurements in the frequency range 10 Hz to 20 GHz," *Phys. Med. Biol.*, vol. 41, pp. 2251-2269, 1996.
- [12] S. Gabriel, R. W. Lau and C. Gabriel, "The dielectric properties of biological tissues: III. Parametric models for dielectric spectrum of tissues," *Phys. Med. Biol.*, vol. 41, pp. 2271-2293, 1996.
- [13] T. Joines, Y. Z. C. Li and R. L. Jirtle, "The measured electrical properties of normal and malignant human tissues from 50 to 900 MHz," *Med. Phys.* vol. 21, no. 4, pp. 547-550, April 1994.
- [14] A. M. Campbell and D. V. Land, "Dielectric properties of female human breast tissue measures *in vitro* at 3.2 GHz," *Phys. Med. Biol.*, vol. 37, no. 1, pp. 193-210, 1992.
- [15] A. J. Surowiec, S. S. Stuchly, J. R. Barr and A. Swarup, "Dielectric properties of breast carcinoma and the surrounding tissues," *IEEE Trans. on Bio. Eng.*, vol. 35, no. 4, pp. 257-263, April 1988.
- [16] S. Chaudhary, R. K. Mishra, A. Swarup and J. M. Thomas, "Dielectric properties of normal and malignant human breast tissues at radioactive and microwave frequencies," *Indian J. of Biochemistry and Biophysics*, vol. 21, pp. 76-79, February 1984.
- [17] R. Peloso, D. T. Tuma and R. K. Jain, "Dielectric properties of solid tumors during normothermia and hyperthermia," *IEEE Trans. Biomed. Eng.*, vol. 31, pp. 725-728, November 1984.
- [18] S. Hagness, A. Taflove and J. E. Bridges, "Three-dimensional FDTD analysis of a pulsed microwave confocal systems for breast cancer detection: design of an antenna-array element," *IEEE Trans. Antennas Propagat.*, vol. 47, no. 5, pp. 783-791, May 1999.
- [19] S. C. Hagness, A. Taflove and J. E. Bridges, "Two-dimensional FDTD analysis of a pulsed microwave confocal system for breast cancer detection: Fixed-focus and antenna-array sensors," *IEEE Trans. Biomed. Eng.*, vol. 45, pp. 1470-1479, Dec. 1998.
- [20] X. Li and S. C. Hagness, "A confocal microwave imaging algorithm for breast cancer detection," *IEEE Microwave and Wireless Components Letters*, vol. 11, pp. 130-132, March 2001.
- [21] E. J. Bond, X. Li, S. Hagness and B. D. Van Veen, "Microwave imaging via space-time beamforming for early detection of breast cancer," *IEEE International Conference on Acoustics, Speech, and Signal Processing*, vol. 3, pp. 2909-2912, May 13-17 2002.
- [22] E. C. Fear and M. A. Stuchly, "Microwave detection of breast cancer," *IEEE Trans. Microwave Theory and Tech.*, vol. 46, pp. 1854-1863, November 2000.
- [23] E. C. Fear and M. A. Stuchly, "Microwave system for breast tumor detection," *IEEE Trans. Microwave Theory and Tech.*, vol. 9, no. 11, pp. 470-472, November 1999.
- [24] E. C. Fear, S. C. Hagness, P. M. Meaney, M. Okoniewski, and M. Stuchly, "Enhancing breast tumor detection with near-field imaging," *IEEE Microwave magazine*, pp.48-56, March 2002.
- [25] M. El-Shenawee, C. Rappaport, E. Miller and M. Silevitch, "3-D subsurface analysis of electromagnetic scattering from penetrable/PEC objects buried under rough surfaces: Use of the steepest descent fast multipole method (SDFMM)," *IEEE Trans. Geosci. & Remote Sensing*, vol. 39, no. 6, pp. 1174-1182, June 2001.
- [26] M. El-Shenawee, C. Rappaport and M. Silevitch, "Monte Carlo simulations of electromagnetic wave scattering from random rough surface with 3-D penetrable buried

- object: mine detection application using the SDFMM," *J. Optical Society of America A*, Vol.18, No. 12, pp.3077-3084, December 2001.
- [27] M. El-Shenawee, "Scattering from multiple objects buried under two-dimensional randomly rough surface using the steepest descent fast multipole method," *IEEE Trans. Antennas and Propagations*, accepted for publication, to appear.
- [28] M. El-Shenawee and C. Rappaport, "Monte Carlo simulations for the statistics of clutter in minefields: AP mine-like target buried near a dielectric object beneath two-dimensional randomly rough ground," *IEEE Trans. Geosci. & Rem. Sensing*, Vol. 40, No. 6, June 2002.
- [29] P. W. Barber, J. F. Owen and R. K. Chang, "Resonant scattering for characterization of axisymmetric dielectric objects," *IEEE Trans. Antten. & Propag.*, vol. AP-30, no. 2, pp. 168-172, March 1982.
- [30] B. L. Merchant, P. J. Moser, A. Nagl and H. Uberall, "Complex pole patterns of the scattering amplitude for conducting spheroids and finite-length cylinders," *IEEE Trans. Antennas Propagat.*, vol. 36, no. 12, pp. 1769-1777, December 1988.
- [31] A. W. Glisson, D. Kajfez and J. James, "Evaluation of modes in dielectric resonators using a surface integral equation formulation," *IEEE Trans. Microwave Theory Tech.*, vol. MTT-31, no. 12, pp. 1023-1029, December 1983.
- [32] D. Kajfez, A. W. Glisson and J. James, "Computed modal field distribution for isolated dielectric resonators," *IEEE Trans. Microwave Theory Tech.*, vol. MTT-32, no. 12, pp. 1609-1616, December 1984.
- [33] J. V. Bladel, "On the resonances of a dielectric resonators of very high permittivity," *IEEE Trans. Microwave Theory Tech.*, vol. MTT-23, no. 2, pp. 199-208, February 1975.
- [34] P. Affolter and B. Eliasson, "Electromagnetic resonances and Q-factors of lossy dielectric spheres," *IEEE Trans. Microwave Theory and Tech.*, VOL. mtt-21, NO. 9, PP. 573-578, September 1973.
- [35] M. Gastine, L. Courtois and J. L. Dormann, "Electromagnetic resonancse of free dielectric spheres," *IEEE Trans. Microwave Theory and Tech.*, VOL. mtt-15, NO. 12, PP. 694-700, December 1967.
- [36] J. V. Bladel, "The excitation of dielectric resonators of very high permittivity," *IEEE Trans. Microwave Theory and Tech*, vol. MTT-23, no. 2, pp. 208-217, February 1974.
- [37] D. J. Burr and Y. T. Lo, "Remote sensing of complex permittivity by multipole resonances in RCS," *IEEE Trans. Antten. & Propag.*, vol. AP-21, no. 4, pp. 554-561, July 1973.
- [38] S. Lin and G. W. Hanson, "An efficient full-wave method for analysis of dielectric resonators possessing separable geometries immersed in inhomogeneous environment," *IEEE Trans. Microwave Theory and Tech.*, vol. 48, no. 1, January 2000.
- [39] N. Geng, D. R. Jackson and L. Carin, "On the resonances of a dielectric BOR buried in a dispersive layered medium," *IEEE Trans. Antennas Propagat.*, vol. 47, no. 8, pp. 1305-1313, August 1999.
- [40] J. R. Arias-Gonzalez, M. Nieto-Vesperinas, and A. Madrazo, "Morphology-dependent resonances in the scattering of electromagnetic waves from an object buried beneath a plane or a random rough surface," *J. Opt. Soc. Am., A*, vol. 16, no. 12, pp. 2928-2934, December 1999.
- [41] V. Rokhlin, "Rapid solution of integral equations of scattering theory in two dimensions," *J. Comput. Phys.*, vol. 36, pp. 414-439, 1990.
- [42] C. C. Lu and W. C. Chew, "A multilevel fast-algorithm for solving a boundary integral equation of wave scattering," *Microwave Opt. Tech. Let.*, vol. 7, pp. 466-470, July 1994.

- [43] V. Jandhyala, *Fast Multilevel Algorithms for the Efficient Electromagnetic Analysis of Quasi-Planar Structures*, Ph.D. Thesis, Department of Electrical and Computer Engineering, University of Illinois at Urbana-Champaign, 1998.
- [44] M. El-Shenawee, V. Jandhyala, E. Michielssen and W. C. Chew, "The steepest descent fast multipole method (SDFMM) for solving combined field integral equation pertinent to rough surface scattering," *Proc. of the IEEE APS/URSI '99 Conf.*, Orlando, Florida, pp. 534-537, July 1999.
- [45] M. El-Shenawee, "The multiple interaction model for non-shallow scatterers buried beneath two-dimensional random rough surfaces," *IEEE Trans. on Geosci. & Remote Sensing*, Vol. 40, No. 4, pp. 982-987, April 2002.
- [46] S. M. Rao, D. R. Wilton and A. W. Glisson, "Electromagnetic scattering by surfaces of arbitrary shape," *IEEE Trans. on Anten. & Propag.*, vol. AP-30, no. 3, pp. 409-418, May 1982.
- [47] L. Medgyesi-Mitschang, J. Putnam and M. Gedera, "Generalized method of moments for three-dimensional penetrable scatterers," *J. Opt. Soc. Am. A*, vol. 11, no. 4, pp. 1383-1398, April 1994.
- [48] C. A. Balanis, *Advanced engineering electromagnetics*, John Wiley & Sons Inc., Ch. 6, pp. 254-309, 1989.
- [49] R. L. Wagner, J. Song and W. C. Chew, "Monte Carlo simulation of electromagnetic scattering from two-dimensional random rough surfaces," *IEEE Trans. Antennas & Prop.*, vol. 45, no. 2, pp. 235-245, February 1997.
- [50] P. Tran and A. A. Maradudin, "Scattering of a scalar beam from a two-dimensional randomly rough hard wall: enhanced backscatter," *Phy. Rev. B*, vol. 45, no. 7, pp. 3936-3939, February 1992.

## List of Figures

**Figure 1.** The relative dielectric constant ( $\epsilon_r = \epsilon' - j\epsilon''$ ) vs the frequency for the normal and malignant breast tissues obtained using equation 1 in Ref. [20].

**Figure 2.** Cross section of a spherical tumor buried beneath (a) a flat air-breast interface showing the multiple interactions mechanism with  $n = 2$ , (b) side view of the 3-D curved breast geometry.

**Figure 3.** Co-polarized backscatter RCS vs the normalized radius  $ka$  for a sphere immersed in air for three cases of relative dielectric constants  $\epsilon_r = 50-j12$ , 50 and 36 at  $\vartheta^i = 0^\circ$  and V-polarization.

**Figure 4.** Co-polarized backscatter RCS vs the normalized radius  $ka$  for just a buried sphere beneath a flat interface (depicted in Fig. 2a) with  $\epsilon_{r1} = 1$  (air) and  $\epsilon_{r2} = 2.0-j0.1$  and  $\epsilon_{r3} = 50$  at two burial depths ( $d = -0.3\lambda_0$  and  $-0.6\lambda_0$ ), H-polarization at  $\vartheta^i = 0^\circ$ .

**Figure 5.** Co-polarized backscatter RCS vs the normalized radius  $ka$  for just the spherical tumor with (a)  $\epsilon_{r2} = 9.0-j1.2$  and  $\epsilon_{r3} = 50-j12$  for breast tissues, (b) with a variety of dielectric constants for the tumor and breast tissues. All results are for  $\vartheta^i = 0^\circ$  and H-polarization.

**Figure 6.** Co-polarized backscatter RCS vs the frequency for just the spherical malignant tumor of dielectric constants varying with the frequency (see Fig. 1) and buried in normal breast tissues with  $\epsilon_{r2} = 10.0-j1.2$ , beneath the flat breast depicted in Fig. 2a at depth (a)  $d = 1\text{cm}$ , (b)  $d = 5\text{cm}$ . All results are for  $\vartheta^i = 0^\circ$  and H-polarization.

**Figure 7.** Co-polarized RCS vs the normalized radius  $ka$  for just the spherical malignant tumor ( $\epsilon_{r3} = 50-j12$ ) buried at  $d = +0.3\lambda_0$  in normal tissues ( $\epsilon_{r2} = 9.0-j1.2$ ) as depicted in Fig. 2b for (a)  $\vartheta^i = 0^\circ$  H-polarization, (b)  $\vartheta^i = 45^\circ$ , H-polarization, (c)  $\vartheta^i = 45^\circ$ , V-polarization.

**Figure 8.** Co-polarized backscatter RCS vs the normalized radius  $ka$  for just the spherical malignant tumor with  $\epsilon_{r3} = 50-j12$ , buried at  $d = +0.3\lambda_0$  in normal breast tissues with  $\epsilon_{r2} = 9.0-j1.2$ , (see Fig. 2b). H-polarization and  $\vartheta^i = 0^\circ$ .

**Figure 9.** Normalized average RCS vs the normalized radius  $ka$  for just the prolate spheroid malignant tumor ( $\epsilon_{r3} = 50-j12$ ) buried in normal breast tissues ( $\epsilon_{r2} = 9.0-j1.2$ ), where  $a = 2b$  for; (a) horizontally oriented prolate spheroid at depth  $d = +0.3\lambda_0$ , (b) randomly oriented prolate spheroid at depth  $d = +0.25\lambda_0$ , (c) the average of (a) and (b) over the three incident directions.

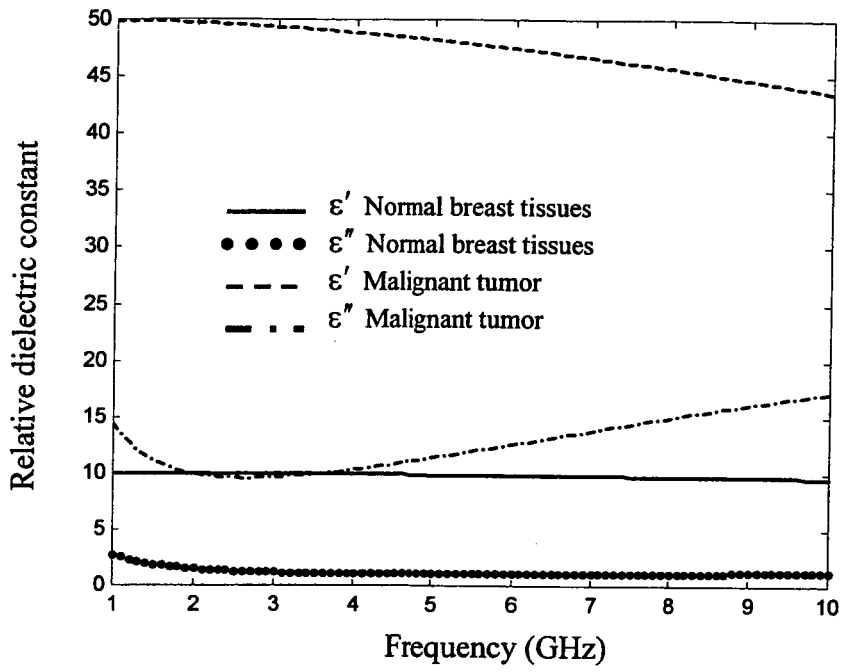
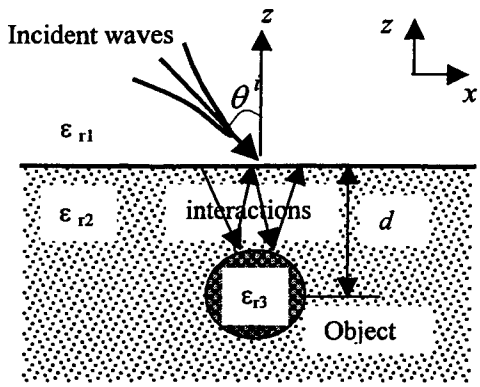
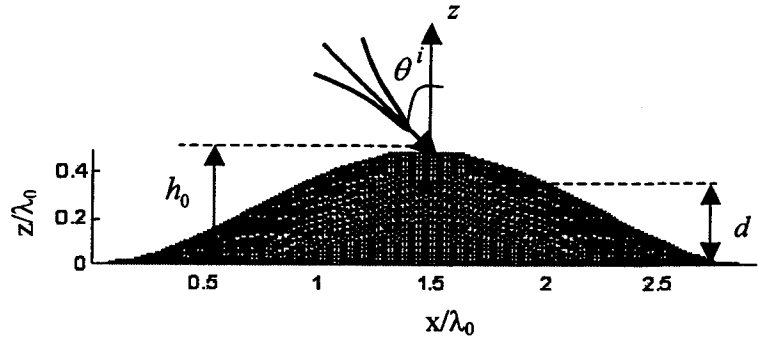


Fig. 1.



(a)



(b)

Fig.2.

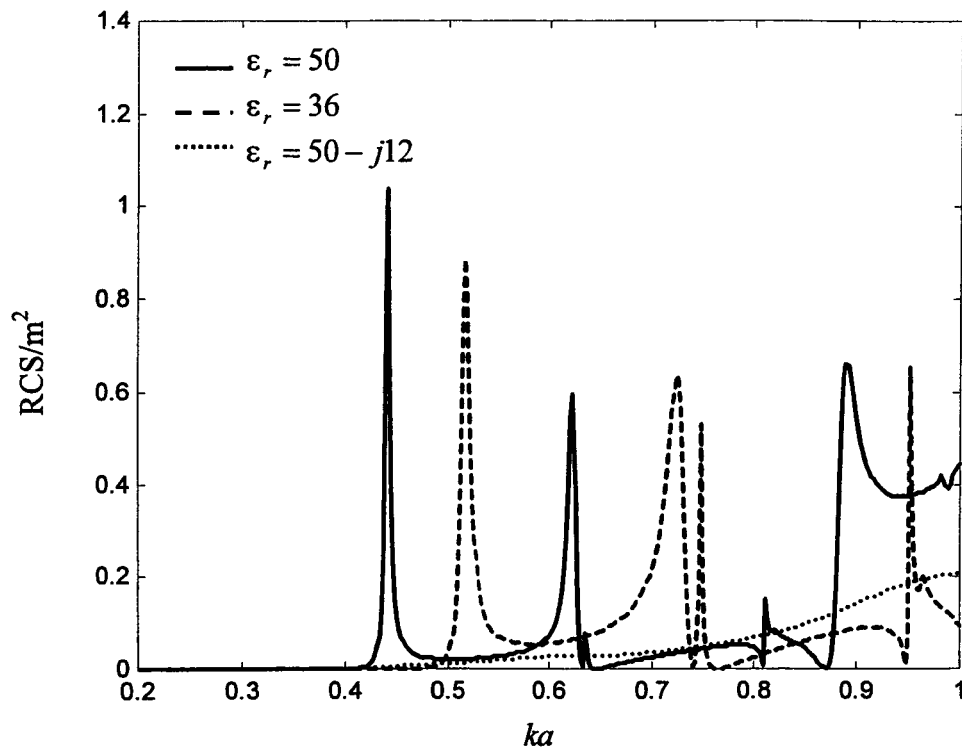


Fig. 3.

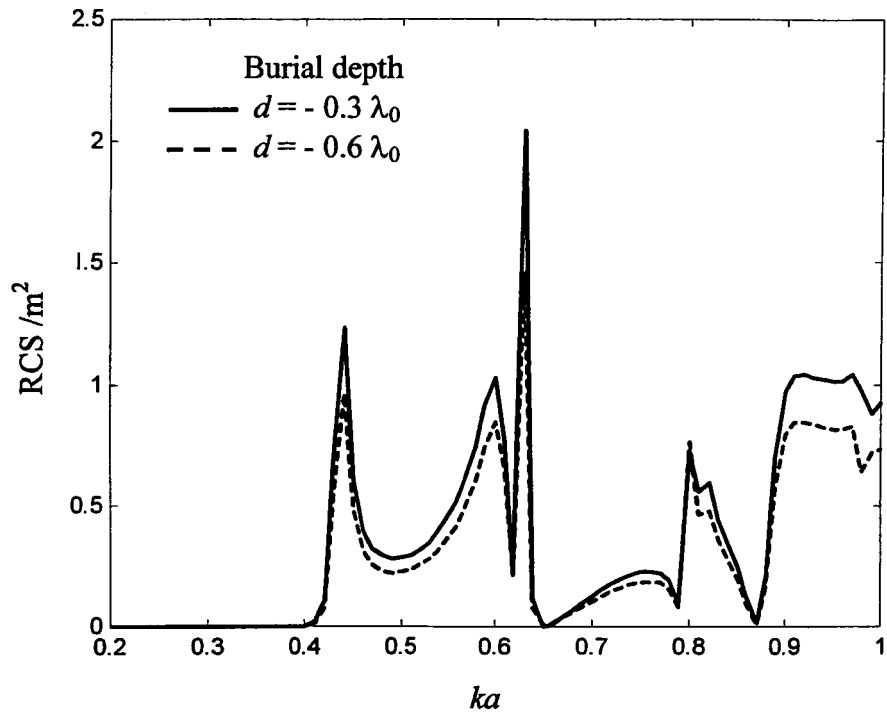


Fig. 4

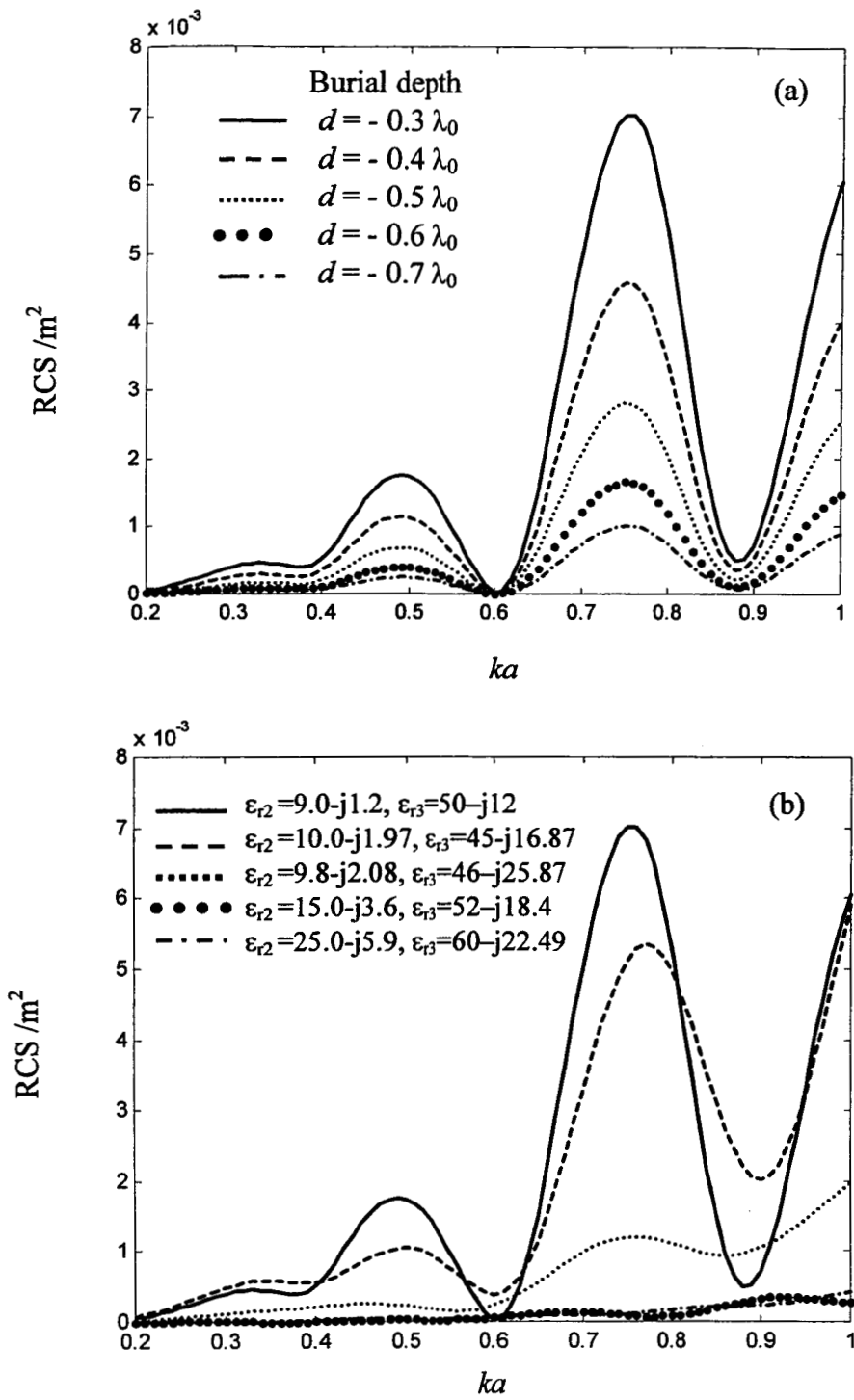


Fig. 5. a-b

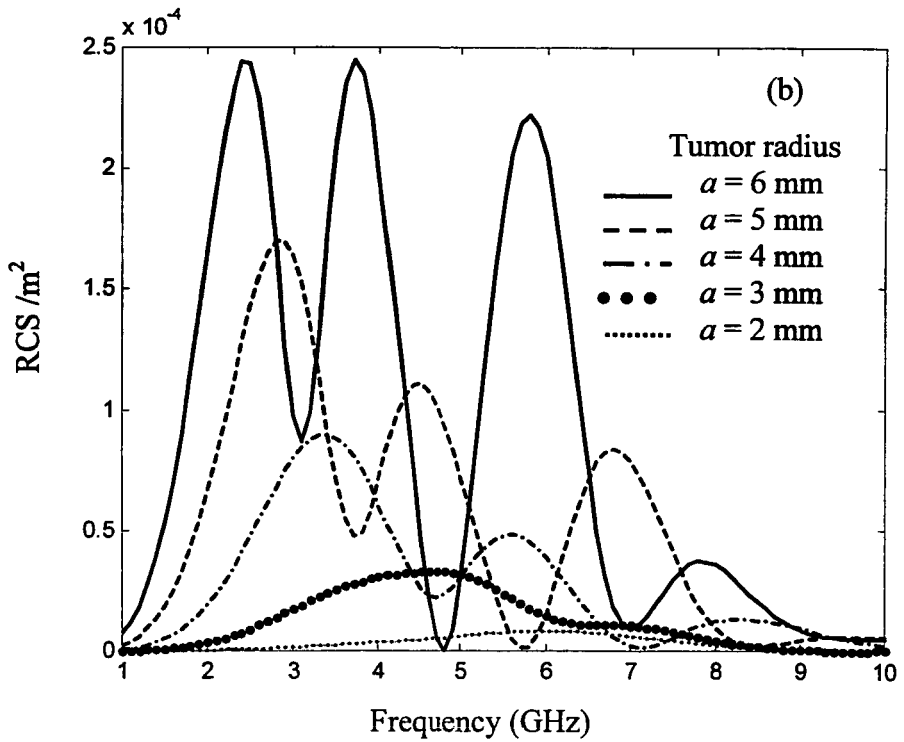
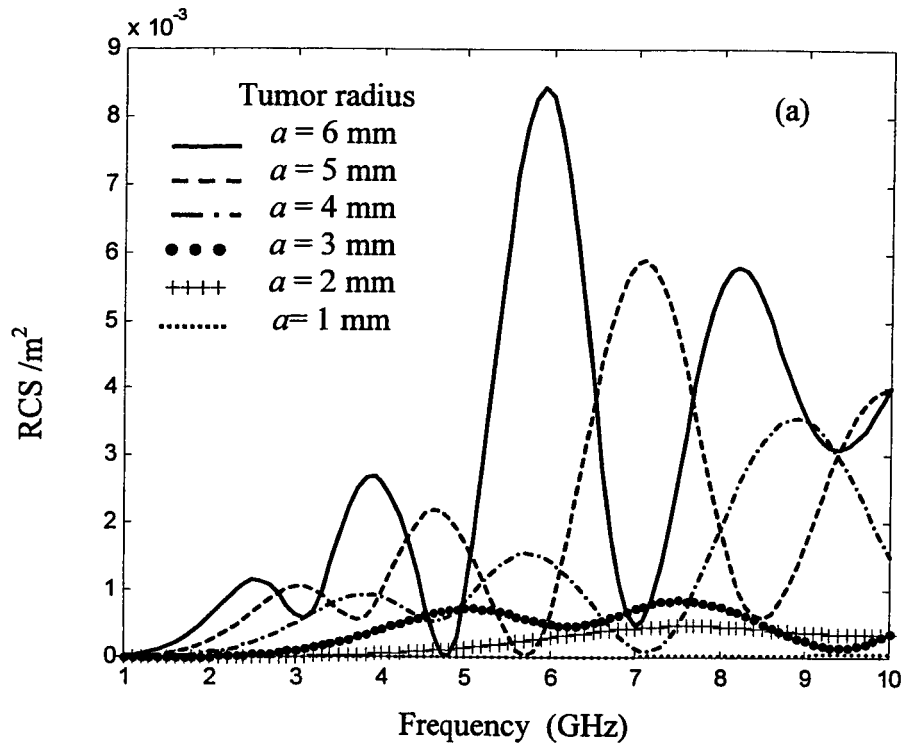


Fig. 6 a-b

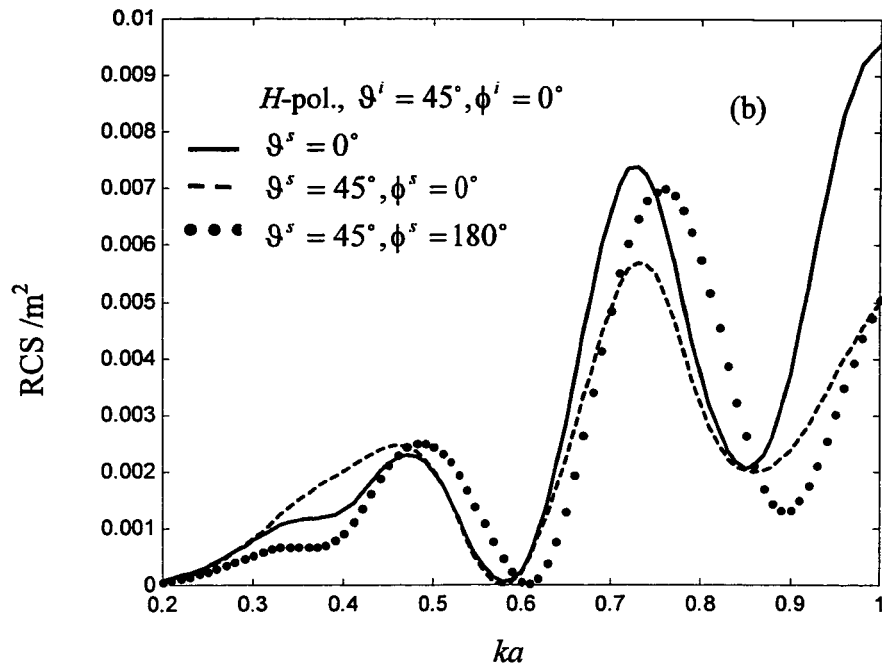
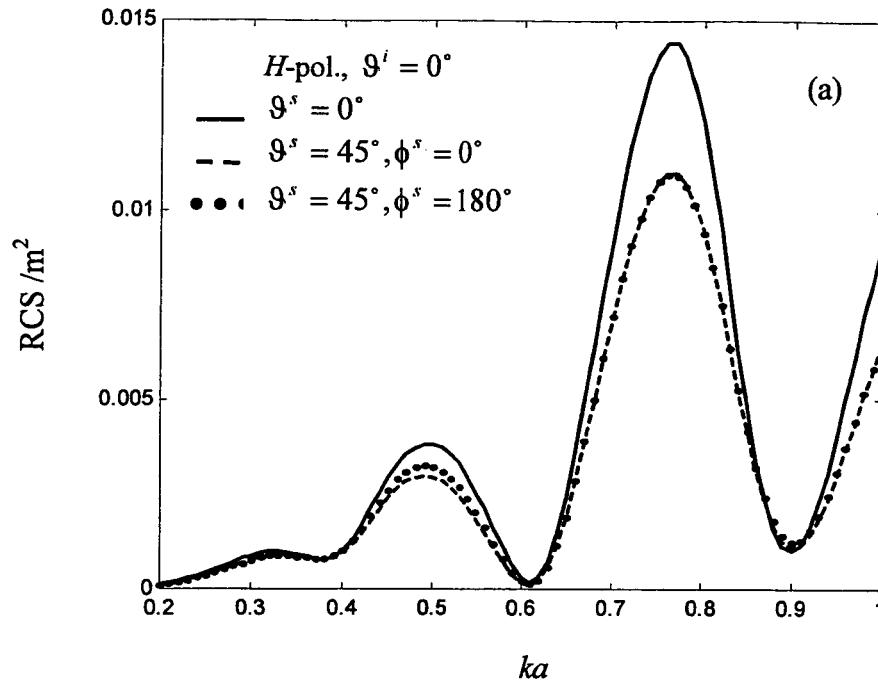


Fig. 7. a-b

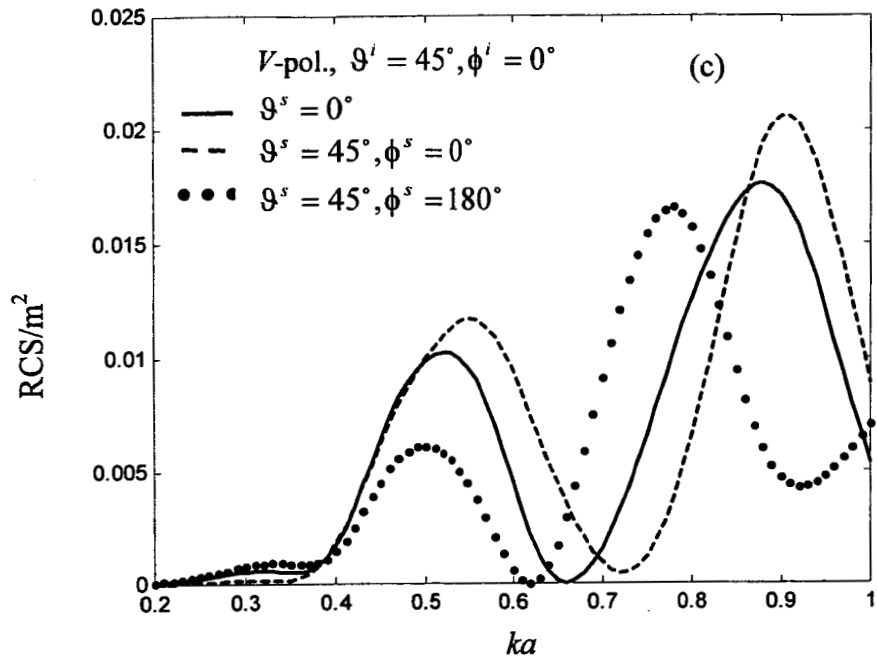


Fig. 7. c

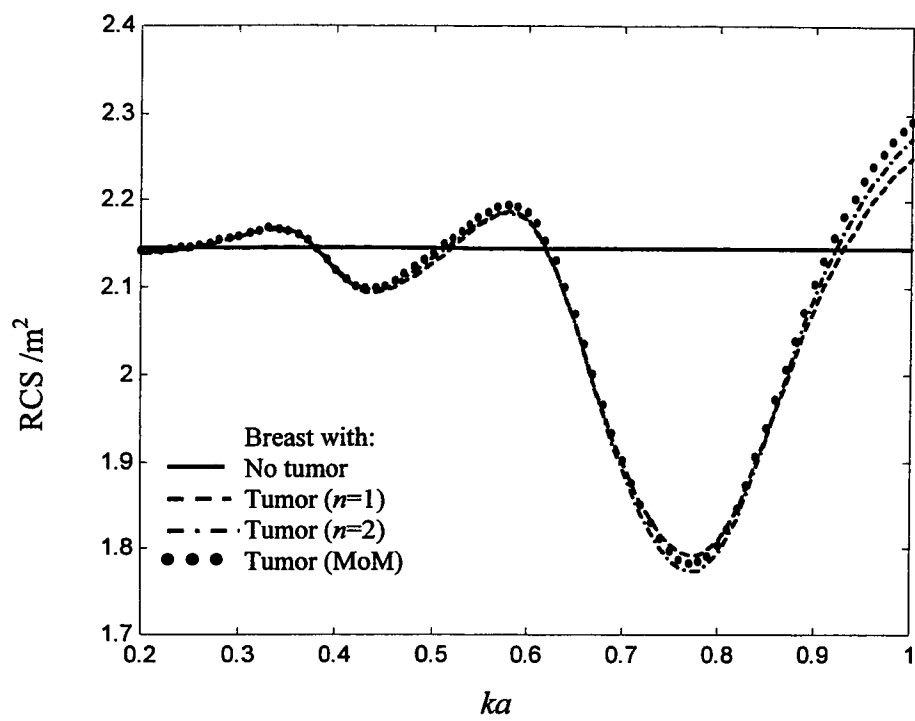


Fig. 8.

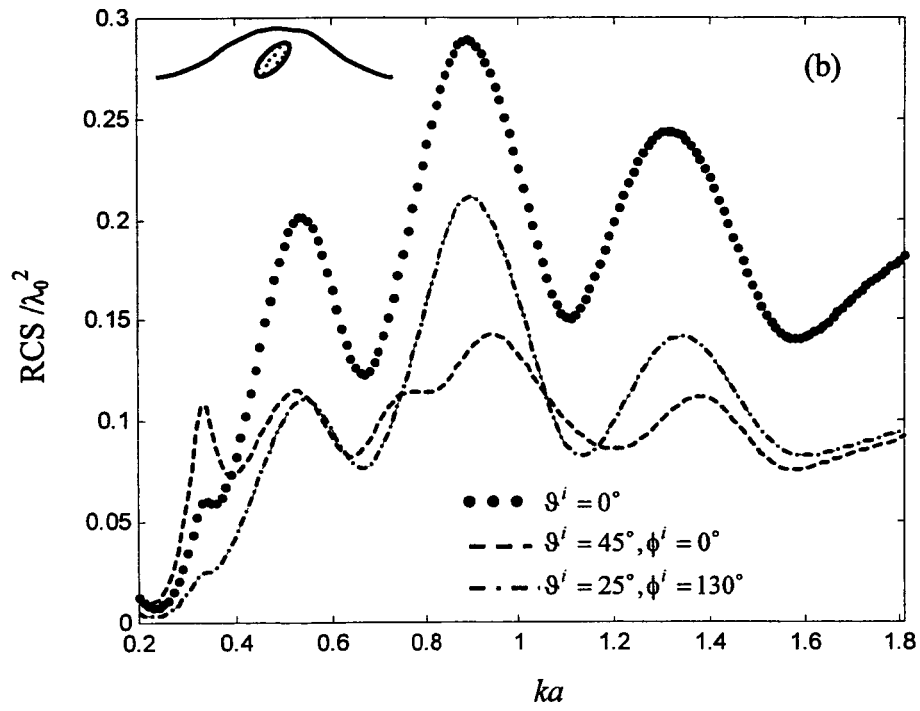
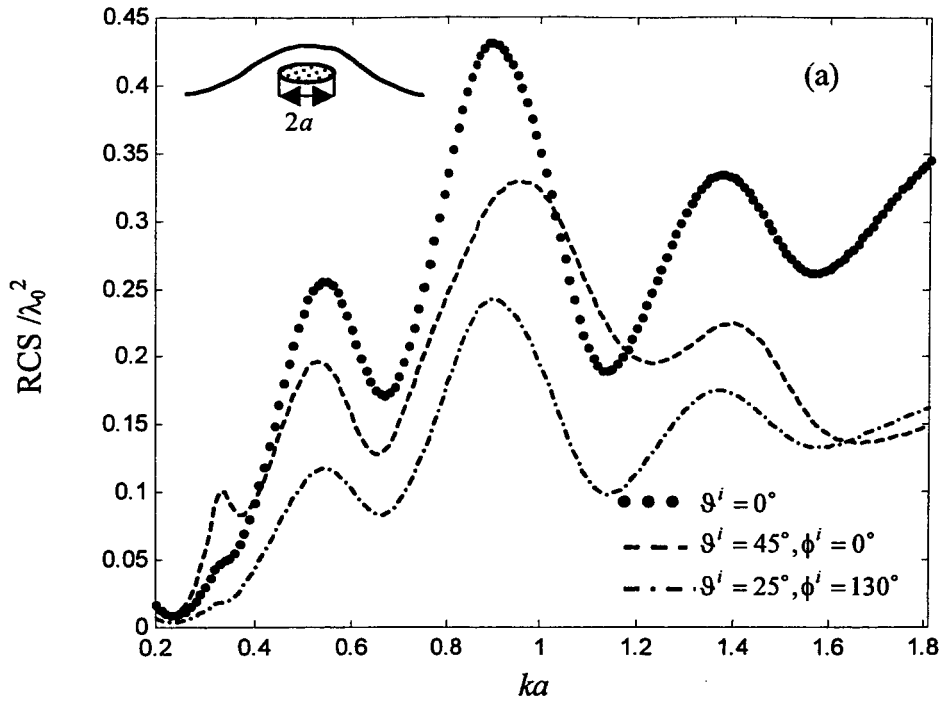


Fig. 9. a-b

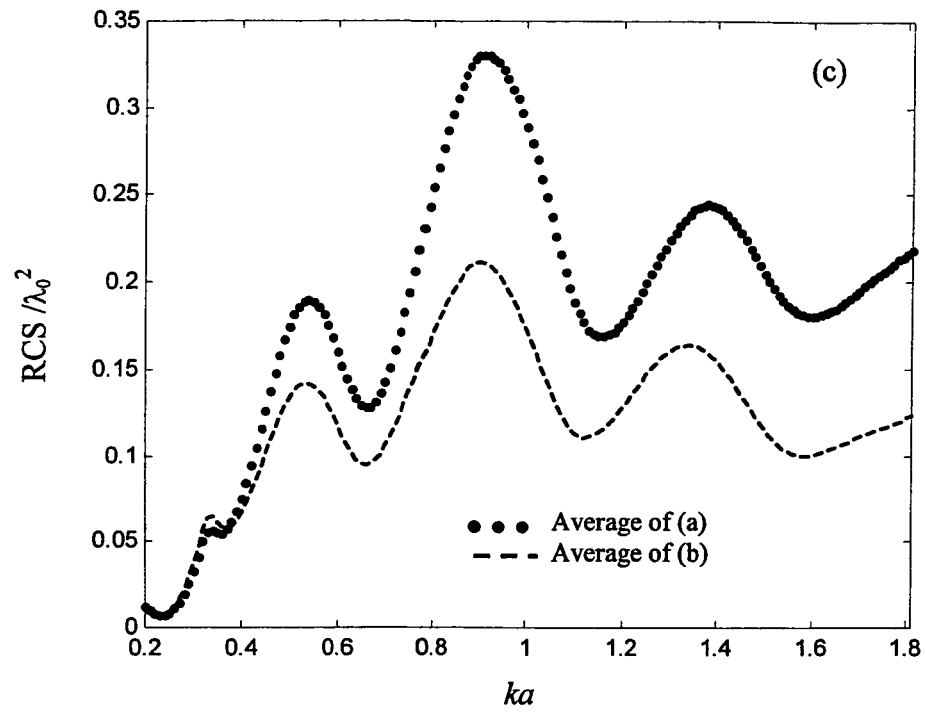


Fig. 9. c

## PART II

# **Numerical Assessment of Multifrequency Microwave Radiometry for Sensing Malignant Breast Cancer Tumor**

Magda El-Shenawee  
Department of Electrical Engineering  
University of Arkansas  
[magda@uark.edu](mailto:magda@uark.edu)

### **Abstract**

A numerical study of microwave radiometry for malignant breast cancer tumor is presented. The numerical results show that the brightness temperature of malignant tumors exhibits a resonant behavior versus the frequency. The brightness magnitude decreases with the tumor burial depth, however, the resonance frequencies depend only on the tumor's size and material and are independent of the burial depth.

**Key words: Radiometry, Breast cancer, Computational EM, Multifrequency, Reflectivity.**

### **I. INTRODUCTION**

Recently, the microwave radiometry has shown potential promise in several subsurface sensing applications [1]-[8]. Numerous work on using multifrequency microwave radiometry was published [2], [3], [8]. In the current work, the emphasis will be on the numerical evaluation of brightness temperature for malignant breast cancer tumor and its behavior as function of frequency.

The basic idea of using microwave radiometry in breast cancer detection is measuring the natural electromagnetic radiation or emission from the female breast at microwave frequencies. This electromagnetic radiation changes considerably with the presence of malignant breast cancer tumors [4]-[8]. In particular, the thermal activity of the female breast is a measure of the tumor growth rate, which can provide information even beyond the physical parameters of the

tumor such as its size, material and location [6]. In [4], the authors presented results based on 618 normal female patients to show the temperature symmetry between the left and right breasts. Therefore, the temperature deviation between the left and right breasts is often used to diagnose the breast cancer in one breast [4]-[6].

As presented and shown in [4]-[6], the medical microwave radiometry has a number of advantages such as the early diagnosis of the cancer before even forming the tumor mass contrast, the non-invasiveness of the technique, the absolute harmless for the patients of all ages, and the range of tumor burial depth is 3-10cm. However, there are some barriers in this technique mainly the required sensitivity of the receiving antenna due to the small-received thermal signals relative to the surrounding noise signals [4]-[6].

The objective of this work is to computationally evaluate the brightness temperature as function of the frequency, tumor size, burial depth and location. The output of this study can be used to understand the thermal radiation phenomenal which will aid in designing enhanced radiometers for breast cancer early detection. The multiple interaction model combined with the fast computational technique, the Steepest descent Fast Multipole Method (SDFMM), [9]-[10] is used here to compute the reflectivity and hence the brightness temperature due to the presence of malignant tumor in the breast.

The geometry of the problem is depicted in Fig. 1, where the breast surface is assumed flat and the tumor is modeled as a sphere of radius  $a$  and buried at depth  $d$  measured from its center. The figure shows the position of the radiometer (applicator) in the near zone to the breast and it shows also the multiple interactions mechanism between the tumor and the breast surface. For simplicity, the thickness of breast skin layer and any interior breast inhomogeneities are not accounted for in this model. A curve fitted data for electrical properties of the malignant tumor

and normal breast tissues are plotted in Fig. 2 versus the frequency range 1-10GHz. These results are based on published experimental measurement data [11].

## II. FORMULATION

The brightness temperature  $T_B$  of an isothermal medium is given by [1], [3]:

$$T_B(\vartheta, \varphi, p, f, \epsilon_{r2}, \epsilon_{r3}, g) = T_s(1 - \Gamma) \quad (1)$$

where the angles  $\vartheta$  and  $\varphi$  are radiometer observation elevation and azimuth angles, respectively,  $f$  is the radiometer observation frequency,  $p$  is the polarization of the radiometer (horizontal  $h$  or vertical  $v$ ),  $\epsilon_{r2}$  is the dielectric constant of the medium,  $\epsilon_{r3}$  is the dielectric constant of the buried object, and  $g$  represents the object geometrical dimensions. The total reflectivity of the medium with buried object is represented with  $\Gamma$ , while the physical temperature of the medium and the object is expressed by  $T_s$  [2].

The power reflection coefficient or reflectivity  $\Gamma$  and the transmissivity  $\Upsilon$  are defined as the normal components of the time-average Poynting's vectors given by [1]:

$$\Gamma = \frac{\hat{z} \cdot \bar{S}_{ar}}{-\hat{z} \cdot \bar{S}_{ai}} \quad (2a)$$

$$\Upsilon = \frac{\hat{z} \cdot \bar{S}_{at}}{\hat{z} \cdot \bar{S}_{ai}} \quad (2b)$$

where  $\bar{S}_a = \text{Re}(\bar{\mathbf{E}} \times \bar{\mathbf{H}}^*)/2$  is the time-average Poynting vector. The subscripts  $r$ ,  $t$  and  $i$  represent reflected, transmitted and incident waves, respectively, and  $\hat{z}$  is a unit vector normal to the flat interface as shown in Fig. 1. In the case of semi-infinite medium with no buried object, the reflectivity and the transmissivity can be obtained in closed forms [1]. In this case, they become functions of the reflection and transmission coefficients upon illuminating the semi-infinite flat interface with plane waves [1], [2].

However, the current problem is different due to the presence of a buried object, i.e. the tumor, in the flat medium, i.e. the breast. The idea here is to computationally evaluate (2a) and (2b) to obtain the reflectivity and transmissivity, respectively, of the whole scatterer (i.e. the medium with the buried object). In this case, the air-flat interface is modeled with a truncated square surface [9], [10] and to eliminate the edge excitations, an incident Gaussian beam is employed. The Gaussian beam is basically is a summation of plane waves tapered towards the surface edges [9], [10]. The size of truncated surface and the incident half beam width should be much larger than the buried object. The total brightness temperature is reformulated to account for the buried object as follows [2]:

$$T_B(\vartheta, \varphi, p, f, \varepsilon_{r2}, \varepsilon_{r3}, g) = T_s(1 - \Gamma_{surf} - P_{obj}^r / P^i) \quad (3a)$$

where the subscripts *surf* and *obj* indicate the interface surface and the buried object, respectively. The total incident power is given by  $P^i$ , the power reflected due to the object only is  $P_{obj}^r$ , and  $\Gamma_{surf}$  is the reflectivity of the flat surface with no buried object. The multiple interaction model presented in [10] is used here to compute the equivalent surface currents on the air-medium interface. These currents can be decomposed into two quantities, one is due to the external excitation and the second is due to the multiple interactions with the tumor (see Fig. 1). The deviation in brightness temperature due to the presence of the tumor is expressed as [2]:

$$\Delta T_B(\vartheta, \varphi, p, f, \varepsilon_{r2}, \varepsilon_{r3}, g) = -T_s(P_{obj}^r / P^i) \quad (3b)$$

The surface currents due to the interactions with tumor is used to compute the reflected power  $P_{obj}^r$  and hence to obtain the deviation in brightness temperature [12]. In practice, this deviation represents the differential in temperature between the left and right breasts to detect the cancer [4]-[6].

### III. NUMERICAL RESULTS

In Example 1, the reflectivity  $\Gamma$  and transmissivity  $\Upsilon$  of a lossless flat medium with no buried object are computed. The relative dielectric constant is assumed  $\epsilon_r = 2.55$  and the truncated surface is assumed  $240\text{cm} \times 240\text{cm}$ . The incident and observed waves are assumed in normal direction for all cases in this section. The objective of this example is to validate the numerical computations of reflectivity and transmissivity obtained using the SDFMM with those obtained using the closed forms for semiinfinite medium excited with plane waves [1]. The ratios of the time-average power densities in (2a) and (2b) are computed using the SDFMM with resolution of 1.2 cm [9], [10], [12]. Briefly, the calculated surface currents on the flat medium are used to radiate electric and magnetic fields at 3cm above and below the interface. No dependency on this distance is observed in the reflectivity or transmissivity for lossless medium. For lossy medium, the fields are compensated with the attenuation factor. However, smaller distances affected the accuracy of the near field calculations [12]. The medium reflectivity and transmissivity are plotted in Fig. 3 versus the  $x$ -direction at  $y = 120\text{cm}$ . Excellent comparison is shown within a square spot of  $150\text{cm} \times 150\text{cm}$  centered at  $x = 120\text{cm}$ ,  $y = 120\text{cm}$ , which is the center of the Gaussian beam footprint. As shown in Fig. 3, the beam width is  $2W = 96\text{cm}$  which implies, as expected, that plane waves can be assumed within the spot area of  $2W \times 2W$ . The reflectivity and transmissivity are added up to unity as shown in Fig. 3. Moreover, at normal incidence, the results for the vertical or horizontal polarizations are similar.

In Fig. 4, the same data of previous example is used and a comparison is shown for the reflectivity and transmissivity but for a slightly lossy medium. The relative dielectric constant here is  $\epsilon_r = 3.55 - j0.4$  (Loamy soil with 5% moisture [1]). Because the computed time-average power densities are obtained at 3cm below the interface as explained earlier, the field values in

this case are multiplied by  $\exp(2\alpha l)$ , where  $\alpha$  is the medium attenuation constant and  $l = 3$  cm. The computed results show excellent agreement with the closed forms in [1] and also within the same spot area  $2W \times 2W$  similar to the previous lossless case.

In Fig. 5, the reflectivity and transmissivity of normal breast tissues with relative dielectric constant  $\epsilon_r = 10 - j1.2$  are computed, see Fig.2 and [11]. Notice that the normal breast tissues have almost the same dielectric constant in the microwave frequency range 1-10 GHz. The results are plotted versus the  $x$ -direction per wavelength and at  $y = 4\lambda_0$ . The modeled surface dimensions are  $8\lambda_0 \times 8\lambda_0$ , where  $\lambda_0$  is the free space wavelength. Also in this example, the computed values of the transmitted fields are multiplied by  $\exp(2\alpha l)$ , with  $l = 0.1\lambda_0$ , the near field resolution is  $0.04\lambda_0$  and the half beam width is  $W = 1.6\lambda_0$ . The reflectivity and transmissivity, upon compensation with the attenuation factor, are added up to unity as shown in Figs. 4 and 5. The reflectivity in Fig. 5 is larger than it in Figs. 3 or 4, which is due to the larger dielectric constant of the medium in this case  $10 - j1.2$ , as shown in Fig. 2. As expected, the transmissivity in Fig. 5 is smaller than it in Figs. 3 or 4 due to the larger conductivity of the medium in this case. Notice the slight oscillations in the transmissivity and reflectivity in Fig. 5, which are due to the increase of edge reflections in this case. This could be decreased by increasing the Gaussian beam tapering, i.e. decreasing  $W$  [9], [10].

In Figs.3-5, a validation is demonstrated in computing the reflectivity and transmissivity using the SDFMM. In Fig. 6, the time-average reflected power density  $\bar{S}_{ar}$  due to only the malignant tumor is plotted versus the  $x$ -direction at  $y = 4\lambda_0$ . The malignant tumor is modeled by a sphere of radius  $a = 5$ mm and is buried at depth of  $d = 2$ cm measured from its center as depicted in Fig.1. The dielectric constant of the malignant tumor is varying with frequency as

shown in Fig. 2, while the dielectric constant of the normal breast tissues is assumed constant as  $\epsilon_r = 10 - j1.2$ . The frequency ranges from 1-5 GHz in steps of 200 MHz, which implies that there are 21 curves plotted in Fig. 6. Notice that the dimension of the plane wave square spot area, as shown in Figs. 3-5, ranges from 96 cm to 19.2 cm. This area is considered much larger than the diameter of the tumor, which is 1cm in this case. The purpose of Fig. 6 is to show that the waves reflected due to the tumor are sensed within the spot area of  $2W \times 2W$  for all considered frequencies. The tumor reflected waves are spherical waves as discussed in [2].

The emphasis of the following examples is to demonstrate the behavior of thermal emissivity or tumor brightness temperature versus frequency. Therefore, in Fig. 7, the reflectivity due to the tumor is plotted versus the frequency from 1-5 GHz in steps of 200 MHz. The tumor radius and burial depth are 5mm and 2cm, respectively. The tumor reflectivity is obtained by computing the term  $(P_{obj}^r / P^i)$  in (3b) which is obtained by integrating the time-average reflected power density  $\bar{S}_{ar}$  due to the tumor and the time-average incident power density  $\bar{S}_{ai}$  of the Gaussian beam over the radiometer cross section area  $A$ , where  $A \leq 2W \times 2W$  as explained in Figs. 3-5. As an example, the radiometer cross section was 1cm $\times$ 2.3cm at 3.3 GHz in [4]. As expected, the total reflected power  $P_{obj}^r$  depends on the cross section area  $A$  of the receiving antenna (i.e. the radiometer or applicator) as shown in Fig. 7a. For simplicity, the radiometer cross section is assumed a square with dimension ranges from  $0.25\lambda_0 - 2\lambda_0$ . The results clearly show the oscillatory behavior of tumor reflectivity versus frequency with peaks occur at 3 GHz and 4.5 GHz. Also, the results show that the smaller the observing area  $A$ , the larger the magnitude of the sensed tumor reflectivity. Upon multiplying the reflectivity of Fig. 7a with the physical temperature  $T_s$ , the deviation in brightness temperature due to the presence of the tumor is shown in Fig. 7b. The physical temperature of breast tissues vary with women's age, e.g. for 50 years

old age, the average temperature of the breast is assumed 33.7 °C (or 306.85 K) as reported in [5]. Naturally, the tumor's physical temperature is different from the surrounding normal breast tissues since they vary in material as shown in Fig. 2. However, in this work it is assumed that the physical temperature  $T_s$  in (3a) and (3b) is the average temperature for the breast which is reported for a variety of ages in [5].

In Fig. 8a and 8b, a parametric study for the brightness temperature deviation  $\Delta T_B$  is investigated versus the frequency with the radiometer cross section area  $A = 0.25\lambda_0 \times 0.25\lambda_0$ . In Fig. 8a,  $\Delta T_B$  is plotted for several burial depths 1–4 cm where the tumor radius  $a$ , is assumed 5 mm. The results show that the brightness temperature oscillates at the same frequencies regardless of the burial depth. However, the brightness magnitude decreases with the burial depth increase due to the large attenuation in normal breast tissues at microwave frequencies. In Fig. 8b,  $\Delta T_B$  is plotted for several tumor radii 2–5 mm buried at the same burial depth of 2 cm. The results clearly show the brightness oscillating behavior for all sizes, however, for larger tumor radius the temperature peaks at lower frequencies and vice versa.

In all above examples, the tumor was buried in the center of the modeled breast at  $(4\lambda_0, 4\lambda_0)$ . In this example, the tumor is buried off center at  $(3.2\lambda_0, 4.8\lambda_0)$ , i.e. in upper left quadrant of the breast. The tumor radius is  $a = 5$  mm and is buried at 2 cm. The deviation in brightness temperature  $\Delta T_B$  is plotted in Fig. 9 for several radiometer square cross section areas with dimensions range as  $0.25\lambda_0 - 3\lambda_0$ . The results show that the brightness temperature increases with the increase of the cross section area up to  $A = 2\lambda_0 \times 2\lambda_0$  and after that it starts to decrease. This observation contradicts the results of Fig. 7b where the brightness temperature increases with the decrease of  $A$ . The reason of this contradiction is that in Fig. 7b both the tumor and radiometer cross section are located at the center of the modeled breast. However, in Fig. 9, the radiometer

location is kept in the breast center, while the tumor is moved to the breast upper left quadrant at  $(3.2\lambda_0, 4.8\lambda_0)$ . This implies that for values of  $A$  smaller than  $1.6\lambda_0 \times 1.6\lambda_0$ , the radiometer does not sense the tumor because it is located outside this area. The radiometer location is experimented and the results show that when it is re-located and centered exactly above the tumor, a greatly enhanced brightness temperature is received. For cross section area equal to  $2\lambda_0 \times 2\lambda_0$ , the exact results of Fig. 7b are obtained. This suggests that scanning breast surface with localized radiometer cross section is better than observing the brightness temperature from the whole breast.

#### IV. CONCLUSIONS

The conducted numerical evaluation for breast cancer tumor's brightness temperature shows clear oscillatory behavior versus the frequency. The results show that the peaks of brightness temperature occur at the same frequencies regardless of the tumor's burial depth, however, the oscillating frequencies depend on the tumor's size and material. These observations can be used to enhance the radiometer design parameters such as the operating frequency or multiple frequencies, the bandwidth and the radiometer receiving cross section area. This statement is considered a future work in collaboration with NASA Langley Research Center.

#### ACKNOWLEDGMENTS

This research was sponsored by the NASA Langley Research Center grant No. US/NASA/NAG-1-020. The author would like to thank Drs. W. Lawrence, J. Johnson, M. Deshpande and W. Munden at NASA Langley for their valuable discussions. This work is supported in part by NSF-ERC Northeastern University award number EEC-9986821.

## REFERENCES

1. Fawwaz T. Ulaby, Richard K. Moore, and Adrian K. Fung, *Microwave Remote Sensing Active and Passive, Volume 1: Microwave Remote Sensing Fundamentals and Radiometry*, Addison-Wesley Publishing Company, 1981.
2. B. Urgan and J. T. Johnson, "A study of microwave thermal emission from a sub-surface object," *Microwave Opt. Tech. Letters*, April 2002.
3. J. T. Johnson, H. Kim, D. Wiggins, and Y. Cheon, "Sub-surface object sensing with a multi-frequency microwave radiometer," accepted in the *IEEE Trans. Geosci. & Rem. Sensing*, to appear.
4. A. H. Barrett, P. C. Myers and N. L. Sadowsky, "Detection of breast cancer by microwave radiometry," *Radio Science*, vol. 12 (68), pp.167-171, 1977.
5. A. V. Vaisblat, S. G. Vesnin, M. A. Konkin, A. V. Lashchenkov and N. N. Tihomirova, "Using Microwave Radiometry for Detection of Breast Cancer," RES. Ltd. Radiometry Company Literature Publisher; [http://www.resltd.ru/eng/literature/cancer\\_eng.htm](http://www.resltd.ru/eng/literature/cancer_eng.htm), 2000.
6. Kenneth L. Carr, "Microwave radiometry: Its importance to the detection of cancer," *IEEE Trans. Microwave Theory and Techniques*, vol. 37, no. 12, pp. 1862-1868, December 1989.
7. J. Lee, K. Kim, S. Lee, S. Eom and R. V. Troitsky, "A novel design of thermal anomaly for mammary gland tumor phantom for microwave radiometer," *IEEE Trans. Biomedical Engineering*, vol. 49, no. 7, pp. 694-699, July 2002.
8. S. Jacobsen and P. R. Stauffer, "Multifrequency radiometric determination of temperature profiles in a lossy homogeneous phantom using a dual-mode antenna with integral water bolus," *IEEE Trans. Microwave Theory and Techniques*, vol. 50, no. 7, pp. 1737-1746, July 2002.

9. M. El-Shenawee, C. Rappaport, E. Miller and M. Silevitch, "Three-dimensional subsurface analysis of electromagnetic scattering from penetrable/PEC objects buried under rough surfaces: use of the steepest descent fast multipole method (SDFMM)," *IEEE Trans. Geosci. & Rem. Sensing*, vol. 39, no. 6, pp. 1174-1182, June 2001.
10. M. El-Shenawee, "The multiple interaction model for non-shallow scatterers buried beneath two-dimensional random rough surfaces," *IEEE Trans. on Geosci. & Remote Sensing*, Vol. 40, No. 4, pp. 982-987, April 2002.
11. X. Li and S. C. Hagness, "A confocal microwave imaging algorithm for breast cancer detection," *IEEE Microwave and Wireless Components Letters*, vol. 11, pp. 130-132, March 2001.
12. C. A. Balanis, *Advanced Engineering Electromagnetics*, John Wiley & Sons Inc, Ch. 6, pp. 254-309, 1989.

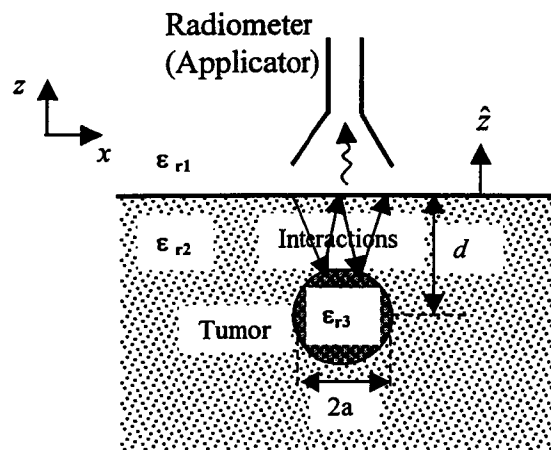


Fig.1. Cross section of a spherical tumor buried beneath a flat air-breast interface showing the multiple interactions mechanism with  $n = 2$ .

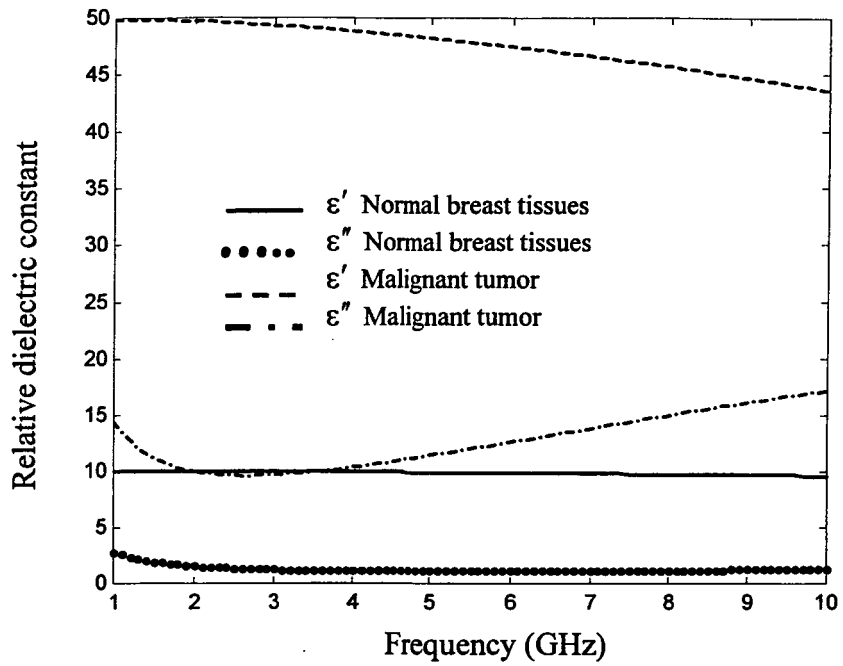


Fig. 2. The relative dielectric constant ( $\epsilon_r = \epsilon' - j\epsilon''$ ) vs frequency for the normal and malignant breast tissues obtained using equation 1 in Ref. [20].

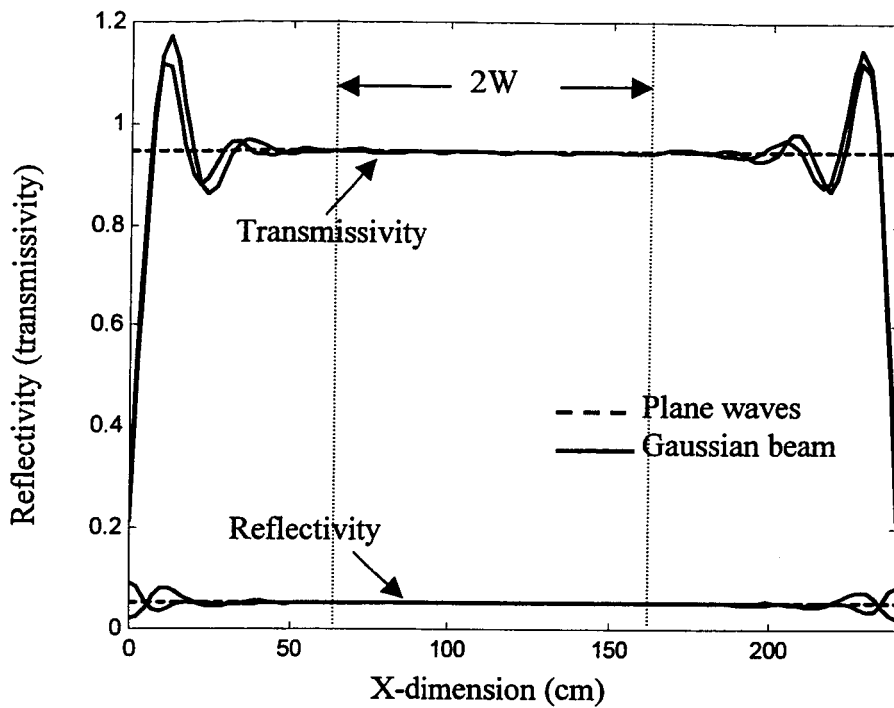


Fig. 3. Reflectivity and transmissivity of a lossless flat medium with relative dielectric constant  $\epsilon_r = 2.55$ . The solid curves represent the SDFMM results for both the vertical and horizontal polarizations and the dotted curves represent the closed forms of the semiinfinite medium.

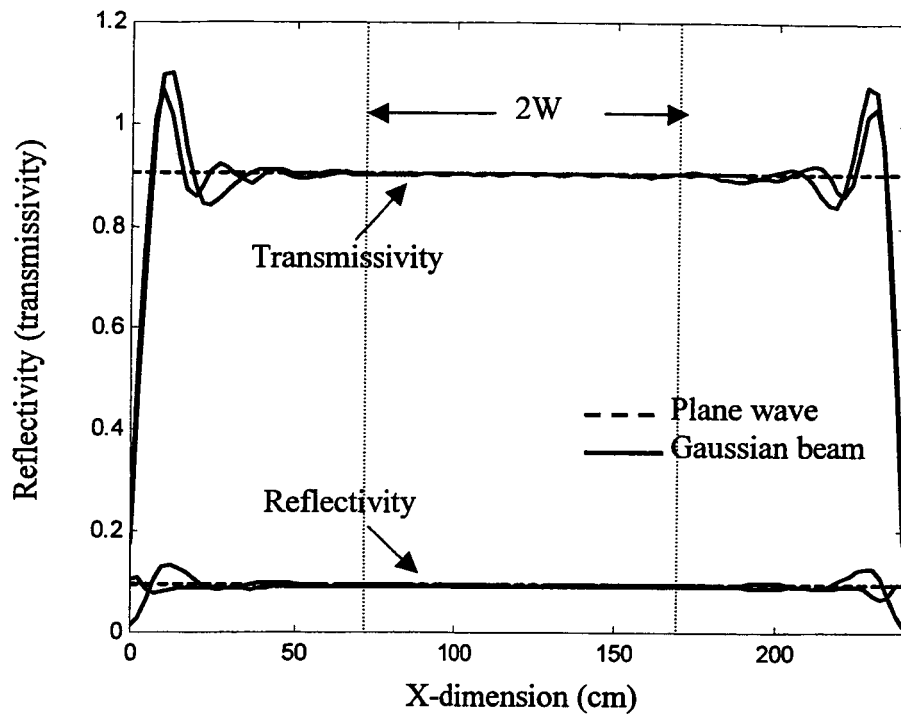


Fig. 4. The reflectivity and transmissivity of a slightly lossy flat medium with no buried object and relative dielectric constant  $\epsilon_r = 3.55 - j0.4$  (Loamy soil with 5% moisture [1]).

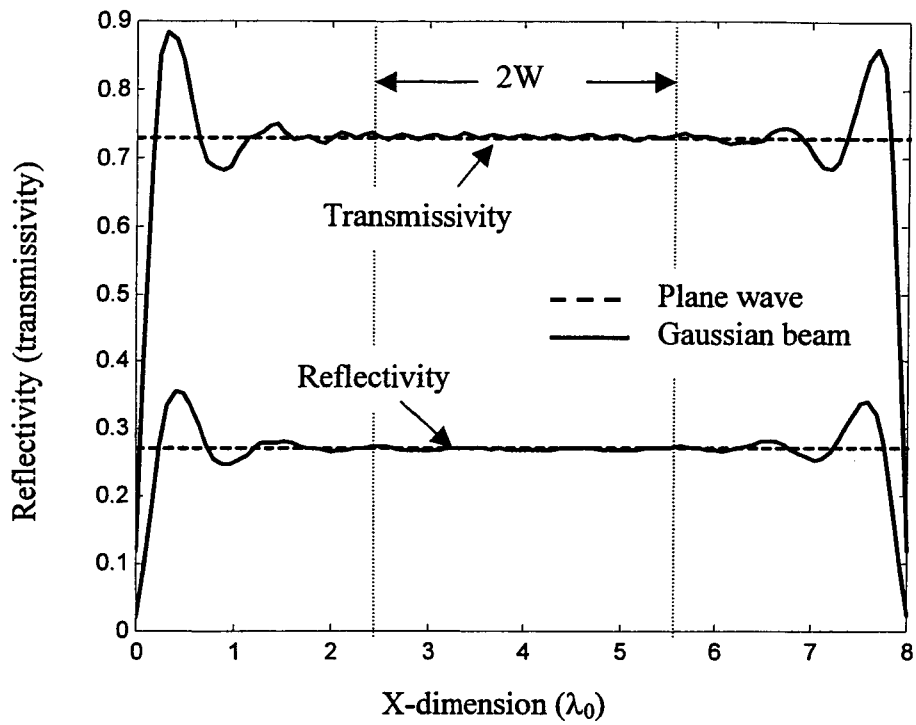


Fig. 5. The reflectivity and transmissivity of normal breast tissues with relative dielectric constant of  $\epsilon_r = 10 - j1.2$  (see Fig.2 and [20]).

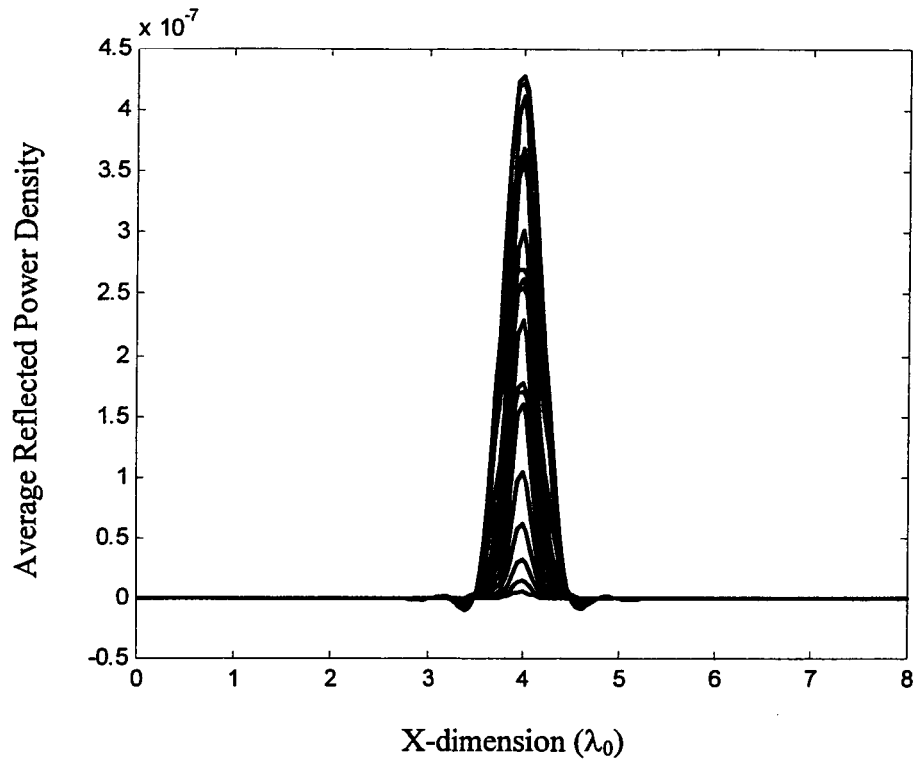


Fig. 6. The time-average reflected power density of the malignant tumor only versus the  $x$ -direction.

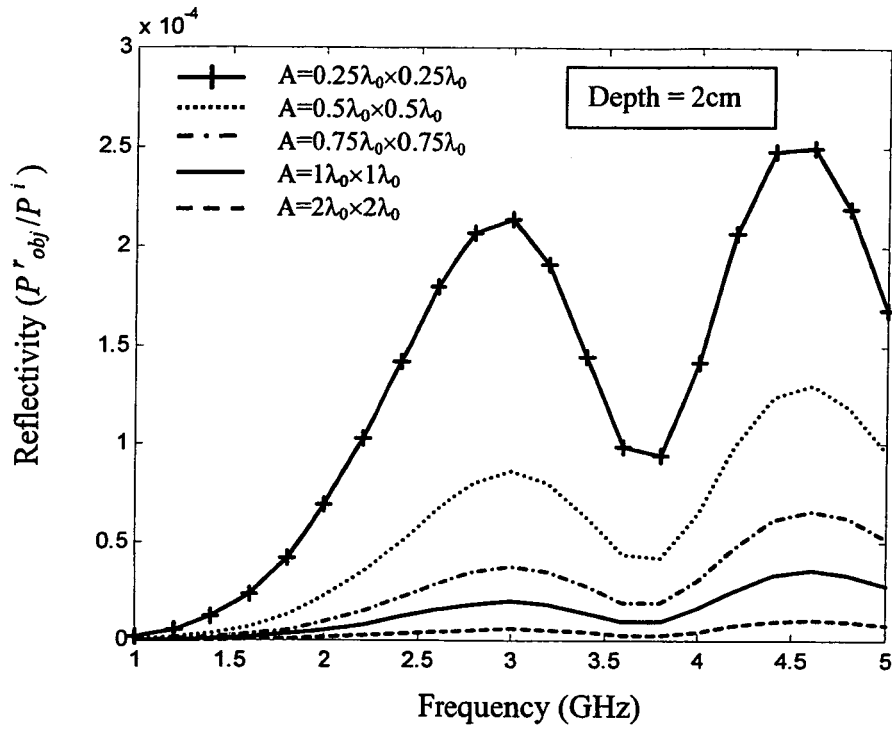


Fig. 7a. The reflectivity of malignant tumor versus frequency. The tumor radius is  $a = 5$  mm and it is buried at depth of 2 cm measured from its center (see Fig. 1).

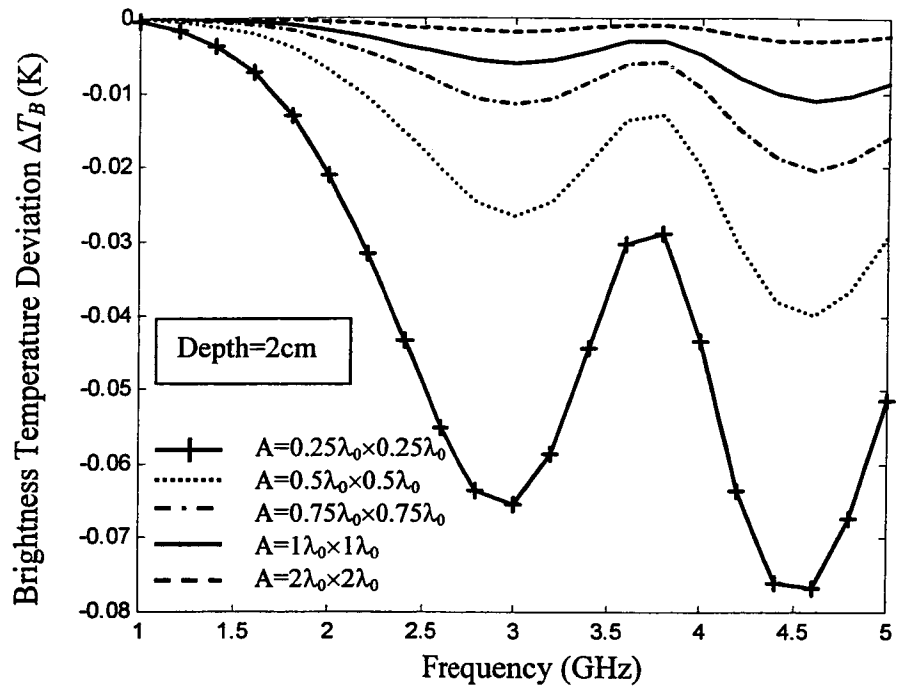


Fig. 7b. Brightness temperature deviation  $\Delta T_B$  due to the presence of malignant tumor of radius  $a = 5\text{mm}$  buried in normal breast tissues for same data of Fig. 7a.

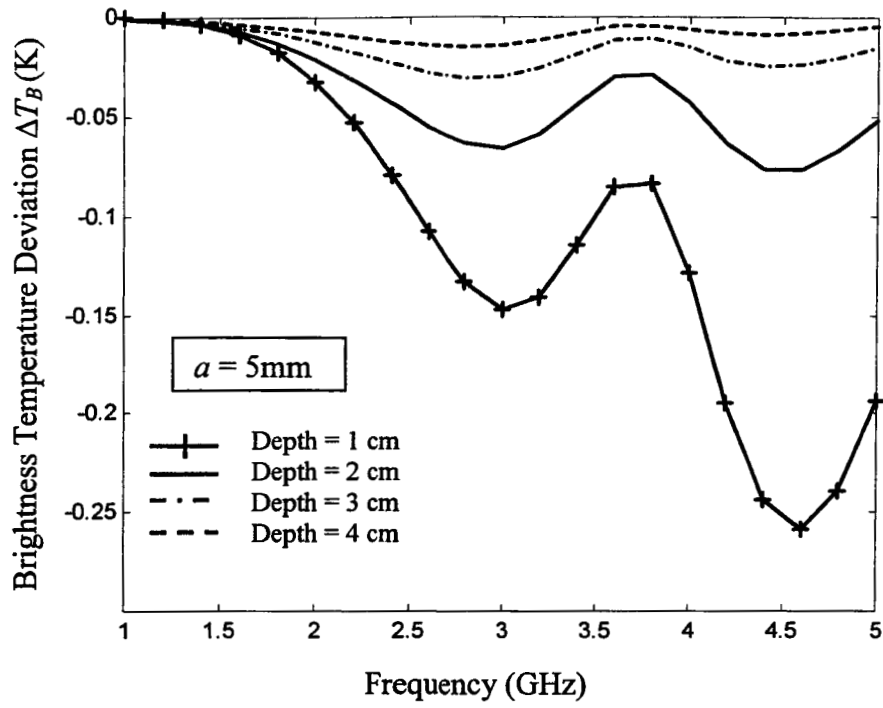


Fig. 8a. Brightness temperature deviation  $\Delta T_B$  due to the presence of malignant tumor in normal breast tissues. The radiometer cross section is assumed as  $A = 0.25\lambda_0 \times 0.25\lambda_0$ .

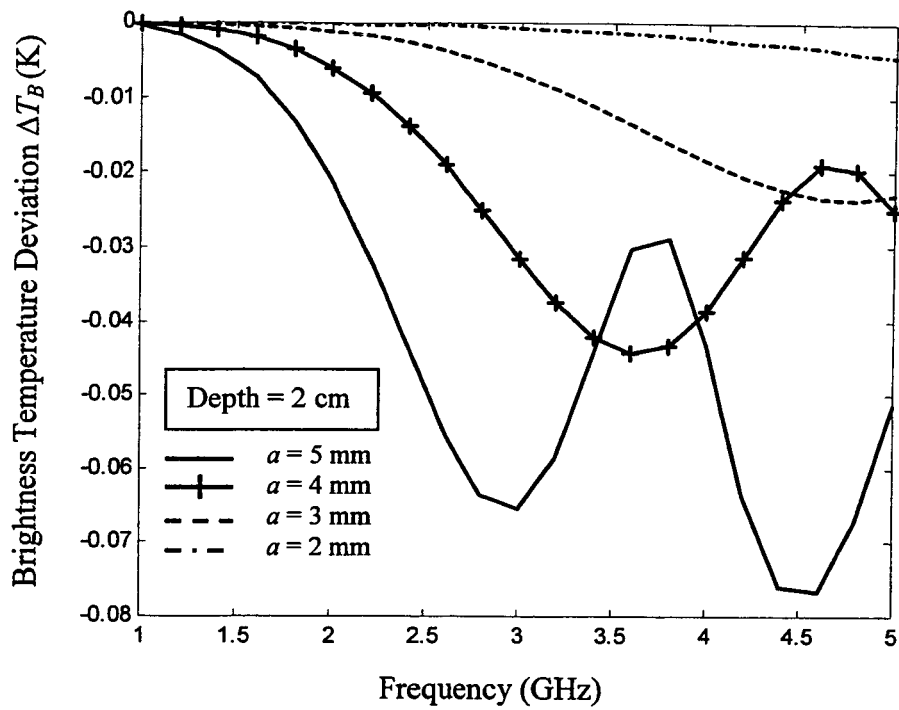


Fig. 8b. Deviation in brightness temperature  $\Delta T_B$  due to the presence of malignant tumor in normal breast tissues. The radiometer cross section area is  $A = 0.25\lambda_0 \times 0.25\lambda_0$ .

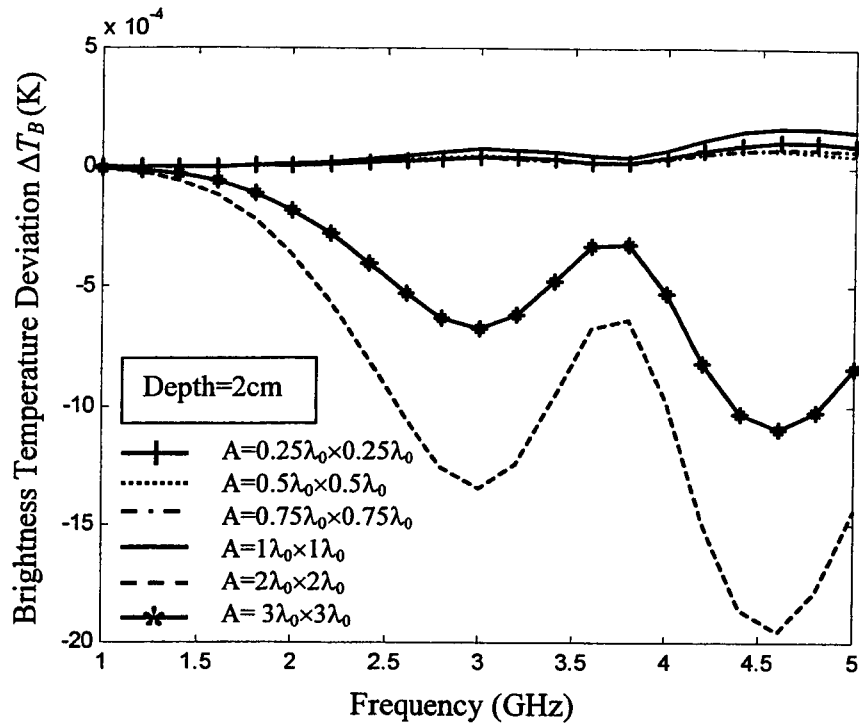


Fig. 9. Deviation in brightness temperature  $\Delta T_B$  due to the presence of malignant tumor in normal breast tissues. The tumor radius is  $a = 5$  mm and is located at  $(3.2\lambda_0, 4.8\lambda_0)$ . The radiometer cross section area  $A$  is centered at  $(4\lambda_0, 4\lambda_0)$ .